

The contrasted phytoplankton dynamics across a frontal system in the southwestern Mediterranean Sea

Roxane Tzortzis¹, Andrea M. Doglioli¹, Monique Messié², Stéphanie Barrillon¹, Anne A. Petrenko¹, Lloyd Izard³, Yuan Zhao⁴, Francesco d'Ovidio³, Franck Dumas⁵, and Gérald Gregori¹

¹Aix Marseille Univ., Université de Toulon, CNRS, IRD, MIO UM 110, 13288, Marseille, France

²Monterey Bay Aquarium Research Institute, Moss Landing, CA, United States

³Sorbonne Université, CNRS, IRD, MNHN, Laboratoire d'Océanographie et du Climat: Expérimentations et Approches Numériques (LOCEAN-IPSL), Paris, France

⁴CAS Key Laboratory of Marine Ecology and Environmental Sciences, Institute of Oceanology, Chinese Academy of Sciences, Qingdao, People's Republic of China

⁵SHOM, Service Hydrographique et Océanographique de la Marine, 13 rue de Chatellier, CS592803, 29228 Brest, CEDEX 2, France

Correspondence: Roxane TZORTZIS (roxane.tzortzis@mio.osupytheas.fr)

Abstract.

~~Phytoplankton plays a major role in the ocean, being the basis of the marine food web and controlling the biogeochemical cycles.~~ Numerical simulations have shown that finescale structures such as fronts are often suitable places for the generation of vertical velocities, transporting subsurface nutrients to the euphotic zone and thus modulating phytoplankton abundance and 5 community structure. ~~Since several years~~ For the past several years, observations have concentrated on nutrient fluxes along these structures. Instead, direct in situ estimations of the phytoplankton growth rates are much less numerous ; although difficult to obtain, they provide a precious information on the ecosystem functioning. Here, we consider the case of a front separating two water masses characterized by several phytoplankton groups with different abundances, in the southwestern Mediterranean Sea. In order to estimate possible differences in ~~growing~~ growth rates, ~~we used an adaptive and Lagrangian sampling strategy~~ 10 ~~to measure the phytoplankton diurnal cycle in these two water masses.~~ we measured the phytoplankton diurnal cycle in these two water masses as identified by an adaptive and Lagrangian sampling strategy. ~~The use of a~~ A size-structured population model was then applied to these data to estimate the growth and ~~division~~ loss rates for each phytoplankton groups identified by flow cytometry, showing that these two population parameters are significantly different on the two sides of the front, and consistent with the relative abundances. Our results introduce a general method for estimating growth rates at frontal systems, 15 paving the way ~~to~~ for in situ exploration of finescale biophysical ~~seenarios~~ interactions.

1 Introduction

~~Phytoplankton is essential for the functioning of the oceans and for the marine ecosystems. Its capacity to perform photosynthesis influences the global carbon cycle, by fixing CO₂ and exporting it either into the ocean depth or to the higher trophic layers through the biological pump (Field et al., 1998; Field et al., 2007). That is why it is primordial to understand the factors that~~

20 rule its abundance and diversity, particularly in the actual context of climate change (Bates et al., 2018). Numerical simulations and remote sensing observations have demonstrated that finescale, i.e. ocean structures characterized by horizontal scale of the order of 1–100 km, with a short lifetime (days–weeks) can play a key role in phytoplankton biological processes. Indeed, the phytoplankton temporal scale is of the same order of magnitude as the one of finescale processes such as eddies, filaments or fronts, suggesting the possibility of a close coupling between phytoplankton growth and finescale forcing. Previous studies
25 have established that finescale frontal structures could induce vertical velocities (Rudnick, 1996), which could modulate the light availability (a change in depth induces a change in irradiance) and drive nutrients in the euphotic layer, thus impacting the abundance and the distribution of phytoplankton communities (e.g. Clayton et al., 2014, Pideoek et al., 2016, Mahadevan et al., 2016, Lévy et al., 2018). Phytoplankton forms the basis of the marine food web (Sterner and Hessen, 1994) and plays a crucial role in biogeochemical processes, including the efficiency of the biological carbon pump, i.e., fixing CO₂ and exporting it into
30 the ocean depth (Field et al., 1998; De La Rocha and Passow, 2007). This process is critical for global ocean sequestration of carbon and therefore for the modulation of atmospheric CO₂. Furthermore, the biological carbon pump is also modulated by the size structure of the phytoplankton community. Small or large phytoplankton species are associated with different efficiencies for particle export, remineralization, and transfer to the deep ocean (Boyd and Newton, 1999; Guidi et al., 2009; Hilligesøe et al., 2011; Mouw et al., 2016, etc). Phytoplankton is also responsible for half of the primary production of the planet (Field
35 et al., 1998), while its biomass is only $\leq 1\%$ of the global biomass (Winder and Cloern, 2010). Thanks to photosynthesis, phytoplankton fuels the ocean in free O₂. That is why, it is primordial to understand the factors that rule phytoplankton abundance and diversity.

"Finescale" refers to ocean dynamical processes induced by mesoscale interactions and frontogenesis (Capet et al., 2008b, a; McWilliams, 2016; Lévy et al., 2018). Finescale structures are characterized by a small Rossby number, horizontal scale
40 of the order of 1–100 km, and a short lifetime (days–weeks). Numerical simulations and remote sensing observations have demonstrated that finescale lifetime is often similar to the phytoplankton growth timescale, suggesting that finescale processes can affect and modulate the phytoplankton community. Different physical processes associated with finescale structures are able to generate vertical velocities, such as deformations of the flow and spatial inhomogeneities (Giordani et al., 2006), eddy perturbation (Martin and Richards, 2001; Pilo et al., 2018), linear Ekman pumping (McGillicuddy Jr et al., 1998; Gaube et al.,
45 2015), or eddy-wind interactions (McGillicuddy Jr et al., 2007). Previous studies have well established that vertical motions impact biogeochemistry (Mahadevan and Tandon, 2006; Mahadevan, 2016; McGillicuddy Jr, 2016). Upward vertical velocities drive deep nutrients into the euphotic layer and also move the phytoplankton cells along the water column resulting in changing light conditions. However, most of the in-situ studies related to the physical-biological coupling at finescale have focused on extreme situations occurring in coastal upwelling regions (Ribalet et al., 2010) and in boundary currents (Clayton et al.,
50 2014, 2017), where intense fronts and dramatic contrasts in water properties are found but are not representative of the global ocean. Indeed, vast oceanic regions are dominated by weak fronts continuously created, moved and dissipated, which separate different water masses with similar properties (Lévy et al., 2018). ~~However, most of the works have focus on the estimation of nutrient fluxes and much less is known about the phytoplankton dynamic across these frontal area. This is due to the rapid evolution of phytoplankton communities across these ephemeral finescale structures, that makes them particularly difficult to~~

55 ~~sample in situ with classical methods of observation.~~ The ephemeral nature of these finescale structures makes them particularly difficult to sample in situ with classical methods of observation. That is why, new sampling strategies were required to track these finescale structures. Some recent cruises have used remote sensing and numerical simulations to define the sampling strategy allowing to target and measure finescale features with physical sensors at high frequency (Shcherbina et al., 2015; Pascual et al., 2017; Petrenko et al., 2017). ~~Concerning the biological variables, although some progress in the understanding of phytoplankton cell cycle has been provided thanks to incubation or sample manipulation (Worden and Binder, 2003), these conventional methods cannot be easily conducted at a daily frequency. A solution is to perform in situ measurements at high frequency (every 20 min) and resolution (1–10 km), thanks to automated analytical flow cytometry, in order to resolve these biological processes at time scales relevant to the cells responses to their environment (Thyssen et al., 2008; Fontana et al., 2018).~~ Concerning the biological variables, although progress in the understanding of phytoplankton cell cycle has been obtained from incubation, sample manipulation (Worden and Binder, 2003) and models (Geider et al., 1997; MacIntyre et al., 2000), performing in situ measurements at high frequency and resolution is a necessity to better understand these biological processes and their responses to the environment. An efficient solution is to lead Lagrangian cruises using automated flow cytometers sampling at high frequency in order to resolve the phytoplankton diurnal cycle in situ, which is challenging using more conventional methods such as cultures or counting by optical microscopy (Thyssen et al., 2008; Fontana et al., 2018).

70 The PROTEVSMED-SWOT cruise was performed in the southwestern Mediterranean Sea, south of the Balearic Islands (Dumas, 2018; Garreau et al., 2020) with the aim to study the physical and biological coupling at finescale. ~~, adopting a Lagrangian adaptive sampling strategy. This approach consists in using remote sensing products (such as sea surface salinity (SSS), temperature (SST), chlorophyll a concentration ([chl a]) and altimetry) to determine the position of oceanic features and guide in quasi-real time the route of the ship and the sampling strategy across these structures of interest. This area is~~ 75 characterized by the presence of both fresh surface waters coming from the Atlantic (AW) and more saline waters from the Mediterranean region (Millot, 1999; Millot et al., 2006). AW enters the Mediterranean Sea through the Strait of Gibraltar and then forms a counterclockwise circulation along the continental slope of the western Mediterranean basin, caused by the combination of the Coriolis effect and the topographical forcing (Millot, 1999; Millot and Taupier-Letage, 2005; Millot et al., 2006). In the southwest part of the basin, this circulation is dominated by the Algerian Current (AC), which can form meanders 80 and mesoscale eddies due to baroclinic and barotropic instabilities (Millot, 1999). These eddies spread over the basin and join the study area south of the Balearic Islands, carrying with them the newly arrived AW, known as younger AW. In this region, the younger AW encounters the older AW sometimes also called resident AW (Balbín et al., 2012) or local AW (Barceló-Llull et al., 2019). The older AW is AW modified by cooling and evaporation during its progression along the northern part of the western Mediterranean basin. The encounter between these two AW often generates finescale frontal structures (Balbín 85 et al., 2014). To our knowledge, except for the works of Balbín et al. (2012, 2014) and the glider experiments of Cotroneo et al. (2016) and Barceló-Llull et al. (2019), very few studies have been performed in this region and these frontal finescale structures have been scarcely sampled due to the difficulty of performing in situ experiments over these short-lived and small features. ~~Thanks to this strategy it was possible to identify~~ During the PROTEVSMED-SWOT cruise a Lagrangian adaptive sampling strategy was performed across a moderately energetic front separating two distinct AW at different stage of mixing

90 (Tzortzis et al., 2021). to highlight its influence on the distribution of the phytoplankton abundances (Tzortzis et al., 2021). As these two water masses had a signature in temperature and salinity, Tzortzis et al. (2021) identified two types of Atlantic Water (AW) at different stage of mixing, separated by the front. The first AW located south of the front is characterized by absolute salinity (S_A) between 37 g kg^{-1} and 37.5 g kg^{-1} , is named corresponding to the younger AW recently entered into the Mediterranean Sea. Whereas the second AW, referred as "older AW", is found North of the front, and is characterized by a higher S_A (37.5 g kg^{-1} to 38 g kg^{-1}). Whereas north of the front, the AW referred to the older AW, is characterized by a higher S_A (37.5 g kg^{-1} to 38 g kg^{-1}). Tzortzis et al. (2021) have also observed contrasted phytoplankton abundances were observed in these two water masses, with the smallest phytoplankton such as *Synechococcus* dominating south of the front in the younger AW, while microplankton was more abundant north of the front in the older AW. This study As a consequence, our previous study constitutes an important improvement in the understanding of the role of frontal structures at finescale on phytoplankton distribution in a moderately energetic ocean. Nevertheless, open questions remain concerning the mechanisms generating the this observed distribution. Is it exclusively driven by the dynamics of the ocean currents ? What is the role of biological processes ? In the present study, we attempt to explain the particular patterns of phytoplankton abundances observed by automated flow cytometry during the PROTEVSMED-SWOT in the frontal structure, using the size-structured population model of Sosik et al. (2003). This model is based on the reconstruction of the diurnal cycle of phytoplankton: 105 during daylight, active individual cells increase in volume due to photosynthesis. The model follows the cells size distribution, and determines the growth and division rates, for a specific functional group determined by flow cytometry (Sosik et al., 2003; Marrec et al., 2018). Several studies have already used this model, but most of them applied it only to *Synechococcus* or *Prochlorococcus* (Ribalet et al., 2010; Hunter et al., 2014; Marrec et al., 2018). An originality of our work is the attempt to apply this model also on the various phytoplankton functional groups identified by flow cytometry. Our approach implies that, 110 except for *Synechococcus* which refer to a taxonomic group (*cyanobacteria*), other flow cytometric groups refer to different range of sizes (estimated from light scatter) and fluorescence intensities related to their photosynthetic pigment content. An other originality of our study is that, to our knowledge, our work is one of the first to apply the model of Sosik et al. (2003) in a context of a Lagrangian sampling strategy to follow two contrasted water masses separated by a front and to study the temporal evolution of their respective phytoplankton communities and dynamics. The objectives of our study are to assess whether 115 the observed contrasted abundances across the front were due to different growth and loss rates. Using high-frequency flow cytometry measurements across the front dividing two water masses, we were able to separately analyze each phytoplankton functional group and reconstruct their biovolume dynamics over a diel cycle in each water mass.

2 Materials and methods

2.1 The Sampling strategy

120 The PROTEVSMED-SWOT cruise, dedicated to the study of finescale dynamics, has been conducted in the south of the Balearic Island between April 30th and May 18th 2018, on board of the RV *Beaumtemps-Beaupré* (Fig. 1a). This site has been chosen in the scope of the future altimetric satellite SWOT (Surface Water Ocean Topography) will launch in 2023. This region

has the advantage of being at the cross-over of two tracks of the satellite during the so-called fast sampling phase dedicated to test and evalval of the satellite (<https://www.swot-adae.org>, last access: April 22, 2023). Furthermore, the Mediterranean sea is a high biodiversity hot spot associated to conditions of oligotrophy and moderate energy, unlike oceanic areas as western boundary currents or eastern boundary upwellings that are largely explored and where the intense dynamics or the large nutrient input can mask the finescale coupled dynamics. The PROTEVSMED-SWOT cruise followed an adaptive and Lagrangian strategy, measuring at high resolution several physical and biological variables with in situ sensors installed both on board (Acoustic Doppler Current Profiler (ADCP), thermosalinograph (TSG), flow cytometer installed on the seawater supply of the TSG) and on a towed vehicle (Seasoar). Tzortzis et al. (2021) provides the detailed description of all the in situ measurements performed during the cruise. In the present study, as we focus on the biological aspects in two contrasted water masses separated by a front, the following description is focused on the sampling strategy as well as the measurements performed by the TSG and the flow cytometer.

Our sampling strategy was both adaptive and Lagrangian, meaning that the vessel route was designed ad-hoc on the basis of daily remote sensing dataset of altimetry-derived currents and ocean color observations to follow and sample the same water masses for some days. In particular, maps of [chl_a] derived from satellite data allowed to identify two water masses, characterized by distinct [chl_a] values and separated by a zonal front at about 38° 30' N (Fig. 1b). This front has also been detected using the in situ horizontal velocities, temperature and salinity, as described by Tzortzis et al. (2021). Once the front localized, repeated transects were performed across the two water masses separated by the front adapting the temporal sampling to the biological time scales in order to reconstruct the phytoplankton 24-hours diurnal cycle for each water mass (Fig. 1e).

The PROTEVSMED-SWOT cruise, dedicated to the study of finescale dynamics, was conducted in the south of the Balearic Islands between April 30th and May 18th 2018, on board the R/V *Beautemps-Beaupré* (Fig. 1a). This cruise followed an adaptive Lagrangian strategy to measure at high spatial and temporal resolution several physical and biological variables with both in situ sensors and analysis of the sea surface water intake. The vessel route was designed ad-hoc on the basis of daily remote sensing dataset provided by the Software Package for an Adaptive Satellite-based Sampling for Oceanographic cruises (SPASSO, <https://spasso.mio.osupytheas.fr>, last access: April 22, 2023). SPASSO used altimetry-derived currents from the Mediterranean regional product (nrt_med_allsat_phy_14) AVISO (“Archiving, Validation and Interpretation of Satellite Oceanographic”, <https://www.aviso.altimetry.fr>, last access: April 22, 2023) and ocean color observations. Chlorophyll a concentrations ([chl_a], level 3, 1 km resolution, MODIS-Aqua and NPP-VIIRS sensors combined (after May 27, 2017) into a new product called MULTI) were provided by CMEMS, “Copernicus Marine Environment Monitoring Service”, <https://marine.copernicus.eu>, last access: April 22, 2023. In addition, CLS provided the surface Chl concentration composite products, with the support of the CNES. They were constructed using a simple weighted average over the previous 5 days of data gathered by the Suomi/NPP/VIIRS sensor. SPASSO generated maps of dynamical and biogeochemical structures in both near real time (NRT) and delayed time (DT). Maps of [chl_a] allowed us to identify two water masses, characterized by distinct [chl_a] values and separated by a zonal front at around 38° 30' N. This front was also detected using in situ horizontal velocities, temperature and salinity, as described in Tzortzis et al. (2021). These two water masses were sampled along a designated route

of the ship, represented in black in Fig. 1b. Special attention was paid to adapting the temporal sampling in order to measure the phytoplankton diel cycle in each water mass. This was achieved by continuously sampling across both water masses along transects. While the ship did not remain in each water mass for 24h, day-to-day variability remained low and measurements from several days were combined into one diel cycle (Fig. 1c). The shape depicted by the ship's track led us to call these areas north-south (NS) hippodrome (bold black line in Fig. 1b) performed between 11 May and 13 May 2018.

2.2 In situ measurements

The sea surface temperature and salinity have been measured by a thermosalinograph (TSG) SeaBird Electronics (SBE) 45, which is an underway sensor able to continuously pump seawater at 3 m (more details about the TSG sensor in Tzortzis et al. (2021)). These two physical variables have been converted into conservative temperature (Θ) and absolute salinity (S_A) using the TEOS-10 standards of McDougall et al. (2012). To sample at high frequency the phytoplankton cells, an automated CytoSense flow cytometer (CytoBuoy b.v.) was installed on board and connected to the seawater circuit of the TSG. A sheath fluid made of 0.1 μm filtered seawater stretched the sample in order to separate, align, center and drive the individual particles (i.e. cells) through a laser beam (488 nm wavelength). Several optical signals were recorded when each particle crosses the laser beam: the forward angle light scatter (FWS) and 90° side-ward angle scatter (SWS), related to the size and the structure (granularity) of the particles. Two distinct fluorescence emissions induced by the light excitation were also recorded, a red fluorescence (FLR) induced by chlorophyll *a* content and an orange fluorescence (FLO) induced by the phycocyanin pigment content.

The CytoUSB software (CytoBuoy b.v.) was used to configure and control the flow cytometer and set two distinct protocols, running sequentially every 30 min. A total of 1164 samples were analysed during the cruise. The first protocol (FLR6) was dedicated to the analysis of the smaller phytoplankton, thanks to a FLR trigger threshold fixed at 6 mV, and a volume analysed set up at 1.5 cm^3 . The second protocol (FLR25) targeted nanophytoplankton and microphytoplankton with a FLR trigger level fixed at 25 mV and an analyzed volume of 4 cm^3 . Data were stored in real time on a computer. Once recorded, they were analysed with the CytoClus software (CytoBuoy b.v.) which retrieves information from the 4 pulse shapes curves (FWS, SWS, FLO, FLR) obtained for every single cell. These curves were then projected into distinct two-dimensional planes (cytograms) by computing the curves integral. Using a combination of various cytograms (e.g., FWS vs. FLR, FLO vs. FLR) allows to determine optimal clusters of cells sharing similar properties. These clusters have been demonstrated in the literature as Phytoplankton functional groups (PFGs) (Dubelaar and Jonker, 2000; Reynolds, 2006; Thyssen et al., 2008; Edwards et al., 2015). The PFGs abundance (cells per cubic centimetre) and average variable intensities are extracted from each sample. Finally, the information on each PFG is fetched in the appropriate protocol (e.g., nanophytoplankton in FLR25), resulting in 582 samples (1164/2). Considering the successive samples acquisition permit to monitor the PFGs dynamics over time and space (Thyssen et al., 2008). The irradiance (wavelengths between 400 and 1000 nm) was also measured during the cruise by a CMP6 pyranometer (Kipp and Zonen; <https://www.campbellsci.fr/emp6>, last access: April 22, 2023).

During the cruise, the irradiance (wavelengths between 400 and 1000 nm) was measured by a CMP6 pyranometer (Kipp and Zonen; <https://www.campbellsci.fr/cmp6>, last access: April 22, 2023). Temperature and salinity were measured by a thermosalinograph (TSG). The TSG was equipped with two sensors: a CTD Sea-Bird Electronics SBE 45 sensor installed in the wet lab, connected to the surface water and which continuously pumped seawater at 3 m depth ; and an SBE 38 temperature sensor 195 installed at the entry of the water intake. The TSG measurements were taken every 30 min, which corresponds to around 2 km spatial resolution at typical ship speeds. The data were converted into conservative temperature (Θ) and absolute salinity (S_A) using the TEOS-10 standards of McDougall et al. (2012). To automatically sample and analyze phytoplankton cells, an automated CytoSense flow cytometer (CytoBuoy, b.v. ; (Dubelaar et al., 1999; Dubelaar and Gerritzen, 2000)) was installed 200 on board and connected to the seawater circuit of the TSG. The flow cytometer sampled the seawater in a dedicated small container called “subsample”. The subsample isolates the seawater every 30 min which allows us to ignore the movement of the ship, while the flow cytometer performed its analysis. Between two consecutive samples the subsample was flushed continuously by the seawater circuit of the ship in order to clean and renew the seawater. A sheath fluid made of 0.1 μm filtered seawater stretched the sample in order to separate, align, center and drive the individual particles (i.e. cells) through a laser beam (488 nm wavelength). Several optical signals were recorded when each particle crossed the laser beam: the forward angle 205 light scatter (FWS) and 90° side-ward angle scatter (SWS), related to the size and the structure (granularity) of the particles. Two distinct fluorescence emissions induced by the light excitation were also recorded, a red fluorescence (FLR) induced by chlorophyll a content and an orange fluorescence (FLO) induced by the phycoerythrin pigment content. The CytoUSB software (Cytobuoy b.v.) was used to configure and control the flow cytometer and set two distinct protocols. The first protocol (FLR6) was dedicated to the analysis of the smaller phytoplankton, using a red fluorescence (FLR) trigger threshold fixed at 6 mV, 210 and a volume analyzed set up at 1.5 mL. The second protocol (FLR25) targeted nanophytoplankton and microphytoplankton with a FLR trigger level fixed at 25 mV and an analyzed volume of 4 mL. The FLR trigger was used to discriminate the red fluorescing phytoplanktonic cells from other particles (such as heterotrophic prokaryotes, nanoflagellates, ciliates, etc.). Recorded data were analyzed with the CytoClus software (Cytobuoy b.v.) which retrieves information from the 4 pulse shapes 215 curves (FWS, SWS, FLO, FLR) obtained for every single cell. These curves were then projected into distinct two-dimensional planes (cytograms) by computing the curves’ integral. Using a combination of various cytograms (e.g., FWS vs. FLR, FLO vs. FLR) allows us to determine optimal cell clusters (i.e. cells sharing similar optical properties). These clusters have been demonstrated in the literature to represent phytoplankton functional groups (PFGs) (Dubelaar and Jonker, 2000; Reynolds, 2006; Thyssen et al., 2008; Edwards et al., 2015; Thyssen et al., 2022). Finally, the PFGs abundance (cells per milliliter) and mean light scatter and fluorescence intensities were extracted from each sample.

220 2.3 The size-structured population model

The size-structured population model described in Sosik et al. (2003) and adapted by Dugenne et al. (2014) was used to estimate the phytoplankton growth and division rates of phytoplankton *in situ*. The cell cycle of phytoplankton alternates between cellular growth during the interphase and division at the end of the mitosis. That is why the phytoplankton cells transit in different size classes following a circadian clock. The size-structured population model is based on this size classes

225 distribution. It stands on the assumptions that (i) cell growth is determined by light exposure, (ii) the probability of a cell dividing depends on its size, (iii) all cells have the same probability to change to another size class, and (iv) a cell divides into two daughter cells, each half the size of the mother cell.

230 To use the model, the light scatter signal recorded for each cell by the flow cytometer must be converted in a size (length) and then in a biovolume (v), using a power law relationship between cell size and FWS (Sosik et al., 2003). The absolute number of cells (N) and proportions of cells in the various size classes (w) were investigated during a 24 h period to follow the transitions of cells in each size class for the m size classes defined in our study. The temporal transitions between size classes are assumed to result from either cellular growth, supported by photosynthetic carbon assimilation, or asexual division (i.e., mitosis). The number of classes m was chosen in order to cover the entire observed biovolume from v_{min} to v_{max} .

235 with $v_{1,2,\dots,i,\dots,m}$ denoting the size classes.

The increase in cell size occurring during the interphase is dependent of the proportion of cells that will grow between t and $t + dt$, noted $\gamma(t)$. This probability is expressed as an asymptotic function depending only on the light intensity necessary to the photosynthesis:

240 with E the irradiance (i.e., the light intensity measured by the pyranometer), E^* the irradiance scaling parameter, and γ_{max} the maximal proportion of cells growing between t and $t + dt$.

However, the decrease of cell size depends on the proportions of cells that will enter mitosis between t and $t + dt$. Indeed, during mitosis, the division of one mother cell generates two daughter cells half the size their mother cell. The proportion of cells entering mitosis is expressed as a function of both time and cell size.

245 with f the normal probability density, v the cell biovolume, δ_{max} the maximal proportion of cells entering mitosis, μ_v the mean of the size density distribution, σ_v the standard deviation (SD) of the size density distribution, μ_t the mean of the temporal density distribution, and σ_t the SD of the temporal density distribution. Note that the decrease of cell size controls the population net growth rates.

The initial distribution of the cell size, $N(0)$, is projected with a time step $dt = 10/60$ h, to construct the normalized size distribution, $w(t)$, over a 24 h period, with \hat{w} standing for model predictions.

The tridiagonal transition matrix, $A(t)$, contains:

1. the stasis probability, expressed as the proportions of cells that neither grew nor divided between t and $t + dt$ (Sosik et al., 2003);
2. the growth probability (γ), expressed as the proportions of cells that grew between t and $t + dt$,
- 255 3. the division probability (σ), expressed as the proportions of cells that entered division between t and $t + dt$.

Depending on the set of optimal parameters (Table 1), the function θ minimizes the Gaussian error distribution between predictions (\hat{w}) and observations (w). Their standard deviations are estimated by a Markov chain Monte Carlo approach that samples θ from their prior density distribution, obtained after running 200 optimizations on bootstrapped residuals.

260 with γ_{max} and δ_{max} the proportions of cells in growing phase and in mitosis, respectively, E^* the irradiance scaling parameter, μ_v and σ_v the mean and the SD of size density distribution, μ_t and σ_t the mean and the SD of temporal density distribution (cf Table 1).

265 Ultimately, the equivalent of the temporal projection of proportions is conducted on the absolute diel size distribution (N) with the optimal set of parameters to estimate population intrinsic growth rates (μ_{size}) on a 24 h period, from which the hourly logarithmic difference of observed abundances is subtracted to obtain the daily average population loss rates (\bar{l}).

270 Since the model allows for any cell to grow, divide or be at equilibrium over the entire integration period (asynchronous populations), the growth rates μ_{size} superior to the median size ratio $\mu_{ratio} = \ln(v_{max}/v_{min})$ (indicative of a synchronous population) are assumed to be well represented.

275 We used the size-structured population model described by Sosik et al. (2003) and adapted by Dugenne et al. (2014) and Marrec et al. (2018), to estimate the in situ growth rates of every phytoplankton group identified by the CytoSense flow cytometer, in the older AW and the younger AW. Before applying the model, we reconstructed a daily cycle of 24 h in the two water masses for each phytoplankton group. We use the term reconstruction because the ship did not spend 24 h in a row in each water mass but sailed along two routes, each forming a sort of racetrack passing alternately through the two water masses (Fig. 1b, 1c). By eliminating the dates and keeping the associated sampling times, the 24-hour diel cycle can be reconstructed for each water body (Fig. 1c). This relies on the hypothesis that the phytoplankton community and dynamics remained similar over the two days, and that hydrology and physics for each water mass remained alike during sampling. We also reconstructed the 24-hour irradiance in the two water masses (Fig. A2), because one of the most important parameters of this model is irradiance, since cell growth is dependent on light exposure due to photosynthesis.

280 The model of Sosik et al. (2003) uses as input the phytoplankton cell volume (biovolume) derived from cell light scatter intensities (FWS) (Eq. 1). Biovolumes were estimated using coefficients previously obtained by measuring a set of silica beads with the flow cytometer following the same settings used for phytoplankton analysis. The coefficients β_0 and β_1 used to convert FWS (arbitrary units, a.u.) to biovolume v (μm^3) were derived from a log-log regression between FSW and silica bead volumes. 285 These methods come from the studies of Koch et al. (1996) and Foladori et al. (2008).

$$v = \exp(\beta_0) \times FWS^{\beta_1} \quad (1)$$

with in our case $\beta_1 = 0.9228$ and $\beta_0 = -5.8702$

290 In the size-structured population model, cells are classified into several size classes according to their dimensions at time t . Classes are logarithmically spaced as follows: for i in $1, 2, \dots, m$ $v_i = v_1 2^{(i-1)\Delta v}$ where Δv is constant and chosen to ensure that size classes cover the entire observed biovolume v , from v_1 to v_m (Fig. 2). For *Synechococcus*, $\Delta v = 1/6$ with Δv constant

and $m = 40$, so that the model size classes encompassed our full measured size distributions (0.0279-2.5209 μm).

At any time t , the number of cells in size classes \mathbf{N} (and \mathbf{w} its corresponding normalized distribution), was projected to $t + dt$

295 via matrix multiplication (Eq. 2):

$$\mathbf{N}(t + dt) = \mathbf{A}(t)\mathbf{N}(t) \quad \text{and} \quad \mathbf{w}(t + dt) = \frac{\mathbf{A}(t)\mathbf{N}(t)}{\sum \mathbf{A}(t)\mathbf{N}(t)} \quad (2)$$

We chose $dt = 10$ min (i.e., 10/60 h) as Sosik et al. (2003) and Dugenne et al. (2014), because for this time step, cells are unlikely to grow more than one size class.

300 $\mathbf{A}(t)$ is a tridiagonal transition matrix that contains:

- 1) γ : the probability of cellular growth
- 2) δ : the probability of cells entering mitosis
- 3) the cells stasis, i.e., the probability for cells to maintain their state (i.e size) in equilibrium during the temporal projection.

305 Probability of cellular growth

The probability of cells growing to the next size class (γ) depends only on the light intensity (irradiance) necessary for photosynthesis, expressed as (Eq. 3):

$$\gamma(t) = \gamma_{max} \cdot (1 - \exp(-E(t)/E^*)) \quad (3)$$

310 γ_{max} : maximum proportion of cells growing (dimensionless quantity)

E : irradiance ($\mu\text{E m}^{-2} \text{s}^{-1}$)

E^* : irradiance normalizing constant ($\mu\text{E m}^{-2} \text{s}^{-1}$)

Probability of cells entering mitosis

315

According to Dugenne et al. (2014), δ expresses a proportion (between 0 and 1) modeled by the combination of two Normal distributions (\mathcal{N}). One is linked to the cell size, the other is linked to the time of cell division. Both imply an optimum, reached at \bar{v} and \bar{t} respectively, for cell division above which the cell size and the timing of division is suboptimal (Eq. 4).

$$\delta(t, v) = \delta_{max} \mathcal{N}(\bar{v}, \sigma_v^2) \mathcal{N}(\bar{t}, \sigma_t^2) \quad (4)$$

320 γ_{max} : maximum proportion of cells entering mitosis (dimensionless quantity)

\bar{v} : mean of the size Normal distribution (μm^3)

σ_v : standard deviation of the size Normal distribution (μm^3)

\bar{t} : mean of the time Normal distribution (h)

σ_t : standard deviation of the time Normal distribution (h)

325

Cells stasis

A third functional proportion is included in the transition matrix $\mathbf{A}(t)$, to represent cell stasis. Since this function illustrates a non-transition, it is modeled by the proportion of cells that neither divided nor grew between t and $t + dt$ (Eq. 5).

330 $[1 - \gamma(t)][1 - \delta(t, v)]$ (5)

Optimal parameters

The set of parameters, θ is estimated by maximum likelihood function, assuming errors between observed \mathbf{w} and predicted $\hat{\mathbf{w}}$ normalized size distributions (Eq. 6, 7, 8). Their standard deviations are estimated by a Markov Chain Monte Carlo approach 335 (Geyer, 1992; Neal, 1993) that sample θ from their prior density distribution, obtained after running 200 optimizations on bootstrapped residuals to approximate the parameter posterior distribution using the normal likelihood. (The likelihood function represents the probability of random variable realizations conditional on particular values of the statistical parameters).

$$\theta = [\gamma_{max}, E^*, \delta_{max}, \bar{v}, \sigma_v, \bar{t}, \sigma_t] = \text{argmin}(\sum(\theta)) \quad (6)$$

$$\sum(\theta) = \sum_t^{t+dt} \sum_{i=1}^m (\mathbf{w}(t) - \hat{\mathbf{w}}(t, \theta))^2 \quad (7)$$

340 $\hat{\mathbf{N}}(t, \theta) = \mathbf{A}(t - dt, \theta) \mathbf{N}(t - dt)$ (8)

$\hat{\mathbf{w}}$ is computed from $\hat{\mathbf{N}}$ following Eq. 2. The fit of the model is quantified using two numbers: the loss rate ($\sum(\theta)$, lower indicates better fit), and the correlation between the observed and modeled mean biovolumes \bar{v}_{obs} and \bar{v}_{mod} over the diel cycle ($\text{corr}(\bar{v}_{obs}, \bar{v}_{mod})$, higher indicates better fit). Table 1 provides the model parameters being optimized.

345 Growth rate and loss rate

Once optimal parameters are identified, the model estimates a population intrinsic growth rate μ_{size} , and a specific loss rate l , integrated over a 24 h period. The method uses the fact that the observed size distribution \mathbf{N} is the result of both growth and

loss processes, while the time projection of the initial size distribution $\mathbf{N}(0)$ using the model, $\hat{\mathbf{N}}$, is only the result of growth processes. The growth rate is calculated at each time step following Eq. 9, and integrated over 24 h. 200 iterations by a Markov Chain Monte Carlo were run to estimate the standard deviation of group-specific growth rates.

$$\mu_{size}(t) = \frac{1}{dt} \ln \left(\frac{\sum_{i=1}^m \hat{N}_i(t+dt)}{\sum_{i=1}^m \hat{N}_i(t)} \right) \quad (9)$$

i : i th size class

$\hat{\mathbf{N}}$: predicted size distribution (cells cm^{-3})

355 m : number of size classes

dt : time step (h)

μ_{size} : growth rates (d^{-1})

An independent growth rate estimation was obtained as $\mu_{ratio} = \ln(\bar{v}_{max}/\bar{v}_{min})$ where \bar{v}_{min} and \bar{v}_{max} are the minimum and 360 maximum of the mean observed biovolume \bar{v}_{obs} over the diel cycle (Marrec et al., 2018). μ_{ratio} represents a minimum estimate of the daily growth rate, that would be observed if cells synchronously only grew from the time \bar{v}_{min} is observed (typically dawn) to the time \bar{v}_{max} is observed (typically dusk), and only divided while \bar{v} decreases. Since the model allows for any cell to grow, divide or be at equilibrium over the entire integration period (asynchronous populations), μ_{size} is expected to be higher than μ_{ratio} . In practice, μ_{ratio} is sensitive to noise in the data and is only provided here as an alternative estimate of the growth 365 rate that does not rely on the model.

The population loss rate l is obtained by difference between the intrinsic growth rate $\mu_{size}(t)$ and the temporal change in logarithmic observed size distribution \mathbf{N} , which represents the net growth rate $r(t) = \mu_{size}(t) - l(t)$ so that:

$$\bar{l} = \int \mu_{size}(t) - \frac{1}{dt} \ln \frac{\mathbf{N}(t+dt)}{\mathbf{N}(t)} \quad (10)$$

370 **3 Results**

3.1 Identification of the phytoplankton functional groups by flow cytometry Moved into Appendices

Up to 9 groups of phytoplankton have been identified on the cytograms (Fig. A1), thanks to their light scatter (forward scatter FWS, and sideward scatter SWS) and fluorescence intensities (red fluorescence FLR, and orange fluorescence FLO). These groups have been called using the conventional names used by flow cytometrists, i.e., some groups relate to taxonomy 375 (Synechococcus, Cryptophytes) while others relate to a range of sizes (picoplankton, nanoplankton) as described by Sieburth et al. (1978). *Synechococcus* (Syn on Fig. A1c) is a prokaryotic picophytoplankton that can be distinguished from the other picophytoplankton owing to its high FLO intensity, induced by phycoerythrin pigment content. *Cryptophytes* (Crypto

on Fig. A1c) were also discriminated from the other groups as they also produce a characteristic orange fluorescence induced by phycoerythrin. Concerning the other phytoplankton groups, 4 eukaryotic picophytoplankton groups were put in evidence: 380 Pico1 (on Fig. A1c) characterized by lower FLR and FLO intensities than *Synechococcus*, Pico2 and Pico3 (on Fig. A1d) with higher FWS, SWS and FLR intensities than Pico1, PicoHFLR (on Fig. A1a) has a high FLR signal induced by chla. We defined 2 distinct nanophytoplankton groups (SNano and RNano) according to their high FLR and FLO intensities. SNano exhibits higher SWS/FWS ratio and SWS intensities than RNano (Fig. A1b and Fig. A1a). Finally, microphytoplankton (Micro) is characterized by the highest FLR and FWS intensities (Fig. A1e).

385 3.2 Spatio-temporal distribution of phytoplankton abundances in the two water masses

The sampling strategy adopted during PROTEVSMED-SWOT enabled us to sample two water masses with different properties. The map of the satellite-derived surface [chl_a] shows higher concentration in the **northern** part of the sampling route, corresponding to **the older** AW, than in the **southern** part, corresponding to **the younger** AW (Fig. 1b). Figure 3 shows the properties of the sea surface water as a function of time (from 11 May 00:00 to 13 May 12:00 UTC) along the sampling route. The 390 older AW is characterized by a colder temperature and higher **values of** salinity than the younger AW. Figure 3 also displays the abundances of each phytoplankton group over these two water masses. *Synechococcus* and Pico2 are the most abundant. They present a clear surface distribution pattern, with high abundances in the warm and low salinity water, corresponding to the young AW. A similar distribution is observed for Pico1, Pico3 and RNano but with lower abundances than *Synechococcus* and Pico2. The abundances of SNano, PicoHFLR and Cryptophyte show less contrasts along the cruise than the previous 395 groups, nonetheless the highest abundances can be distinguished in the younger AW, in particular **in during** the second and third passage (transect) across this water mass. Finally, microphytoplankton is the less abundant group, but it clearly shows a contrast between the two water masses, opposite to **the one that** of the other phytoplankton groups.

3.3 Phytoplankton cellular growth and division in the two water masses

The phytoplankton diurnal cycle was reconstructed in the two water masses using the size-structured population model (Sosik 400 et al., 2003) to address the phytoplankton dynamics. We talk about reconstruction because the ship did not spend 24 h in a row in each water mass but sailed along two routes, each forming a sort of racetrack passing alternately through the two water masses. This adaptive Lagrangian approach allows sampling of the different functional groups of phytoplankton in each water mass (Fig. 1b). By eliminating the dates and keeping the associated sampling times (Fig. 1e), the 24-hour nocturnal cycle can be 405 reconstructed for each water body. That relies on the hypothesis that the phytoplankton community and dynamics are the same on the two days, and that hydrology and physics for each water mass remain alike during sampling. We have also reconstructed the 24-hour irradiance in the two water masses represented by the red lines on Fig. 4, 5, 6. Indeed, one of the most important parameters of this model is irradiance, since cell growth is dependent on light exposure due to photosynthesis. Figures 4, 5, 6 represent the phytoplankton size distribution (i.e., biovolume) observed in situ and predicted by the model over 24 h for *Synechococcus*, RNano and SNano respectively. We also attempted to model the diurnal cycle for the picophytoplankton 410 groups, i.e., Pico1, Pico2, Pico3, PicoHFLR. However, we obtained very noisy size distributions and could not obtain a valid

measurement of the growth rates, hence these distributions are not considered further in this study. As microphytoplankton and Cryptophytes were not abundant enough to allow a reliable determination of their abundances and cell cycles, they were not taken into consideration in this study. The reconstruction of the circadian cycle shows that irradiance is almost the same in the two water masses (Fig. 4, 5 and 6, red lines), and the computation of daily total irradiance with a trapezoidal integration give 415 intensities of 286 and 299 $\mu\text{E m}^{-2} \text{s}^{-1}$ for the older AW and the younger AW, respectively (Fig. A2).

Furthermore, the comparison between the biovolume observed *in situ* and the biovolume predicted by the model is sound and confirms that the model-predicted cell-size distributions well recapitulated the diurnal cycle reflecting either growth or cell division. From the predicted biovolume it is possible to derive a specific growth rate (μ_{size}) and a loss rate (l) for both populations in the two water masses. Table 2 summarizes the growth and loss rates found for the different phytoplankton 420 groups in the two water masses. For *Synechococcus*, in the older AW the observed size distribution (i.e., observed biovolume) is similar to the prediction of the model (i.e., predicted biovolume). Both display a day-long large size-class distribution centered approximately on $0.3 \mu\text{m}^3$. In the younger AW (Fig. 4a, 4c) the distributions of observed and predicted biovolume are narrower than in the older AW and centered approximately on $0.2 \mu\text{m}^3$ (Fig. 4b, 4d). The older AW is populated by larger 425 cells of *Synechococcus* (mean biovolume $v_{mean} = 0.38 \pm 0.27 \mu\text{m}^3$) than in the younger AW, (mean biovolume $v_{mean} = 0.21 \pm 0.13 \mu\text{m}^3$). Furthermore, in the older AW, the large cells of *Synechococcus* have a growth rate $\mu_{size} = 0.25 \pm 0.91 \text{ d}^{-1}$ and a loss rate $l = -0.64 \text{ d}^{-1}$, whereas in younger AW the smaller cells are characterized by a high growth rate ($\mu_{size} = 0.71 \pm 1.40 \text{ d}^{-1}$) and a low loss rate ($l = -0.21 \text{ d}^{-1}$). Concerning RNano, the cell size distribution between the older AW (Fig. 5a, c) and the younger AW (Fig. 5b, d) is less contrasted than for *Synechococcus* (Fig. 4). Indeed, we cannot observe a significant difference 430 between the biovolumes, which are equal to $61.9 \pm 20.6 \mu\text{m}^3$ and $59.3 \pm 21.2 \mu\text{m}^3$ in the older AW and in the younger AW, respectively. Furthermore, compared to *Synechococcus*, the RNano growth rates are generally low (Table 2). However, the loss 435 rates of RNano are high, especially in the younger AW ($l = -1.32 \text{ d}^{-1}$) in comparison to the older AW ($l = -0.87 \text{ d}^{-1}$). The size distribution of SNano is similar to those of the other phytoplankton described previously (Fig. 6). Indeed, the older AW is predominantly composed of large SNano cells ($v_{mean} = 84.8 \pm 43.4 \mu\text{m}^3$), compared to the younger AW ($v_{mean} = 60.6 \pm 35.3 \mu\text{m}^3$). Furthermore, the highest values of SNano biovolume and loss rate are found in the older AW, as observed for RNano.

435

The phytoplankton diurnal cycle was reconstructed in the two water masses using the size-structured population model originally developed by Sosik et al. (2003). Figures 4, 5, 6 represent the phytoplankton size distribution (i.e., biovolume) observed 440 in situ and predicted by the model over 24 h for *Synechococcus*, RNano and SNano, respectively. From the predicted biovolume it is possible to derive specific growth (μ_{size}) and a loss (l) rates, summarized in Table 2 for the different phytoplankton groups in the two water masses, along with metrics of model performance. We also attempted to model the diurnal cycle for the picophytoplankton groups, i.e., Pico1, Pico2, Pico3, and PicoHFLR. However, their very noisy size distributions prevented us from obtaining reliable growth rate estimates. Similarly, microphytoplankton and Cryptophytes were not abundant enough to allow a reliable determination of their abundances and cell cycles. These cytometric groups are thus not considered further in this study.

445 For *Synechococcus*, in the older AW the prediction of the model (i.e., predicted biovolume) is similar to the observed size distribution (i.e., observed biovolume). Both display a day-long large size-class distribution centered approximately on 0.3 μm^3 . In the younger AW (Fig. 4a, c) the distributions of observed and predicted biovolume are narrower than in the older AW and centered approximately on 0.2 μm^3 (Fig. 4b, d). As a consequence, the older AW is populated by larger cells of *Synechococcus* (mean observed biovolume $\bar{v}_{obs} = 0.38 \pm 0.04 \mu\text{m}^3$) than in the younger AW (mean biovolume $\bar{v}_{obs} = 0.21 \pm 0.04 \mu\text{m}^3$) (Table 2). Growth and loss rates also differ between the two water masses. In the older AW, the large cells of *Synechococcus* have a growth rate $\mu_{size} = 0.24 \pm 0.91 \text{ d}^{-1}$ and a loss rate $l = 0.36 \text{ d}^{-1}$, whereas in younger AW the smaller cells are characterized by higher growth ($\mu_{size} = 0.68 \pm 1.56 \text{ d}^{-1}$) and loss ($l = 0.48 \text{ d}^{-1}$) rates.

450 Relative to *Synechococcus*, cell size distribution and growth and loss rates are less contrasted between the older and younger AW for SNano (Fig. 6) and even more so RNano (Fig. 5). The mean observed RNano biovolumes are similar in the older and 455 younger AW ($63.5 \pm 2.67 \mu\text{m}^3$ and $61.2 \pm 5.23 \mu\text{m}^3$, respectively) (Table 2). For SNano, similar to *Synechococcus*, the older AW is predominantly composed of larger cells ($\bar{v}_{obs} = 85.0 \pm 1.98 \mu\text{m}^3$) than in the younger AW ($\bar{v}_{obs} = 63.8 \pm 4.45 \mu\text{m}^3$). For both Nano groups, growth rates are generally very low in both water masses ($\mu_{size} < 0.1 \text{ d}^{-1}$). Loss rates are higher than growth rates, except for RNano in the younger AW (negative loss rate implying an external input of cells such as by advection). However, the corresponding optimization factor is the highest observed across the 6 modelisations, indicating this result is 460 subject to caution.

4 Discussion

4.1 The phytoplankton diurnal cycle

Although it has been clearly demonstrated that phytoplankton plays a fundamental role in the ocean ecosystem functioning (Watson et al., 1991; Field et al., 1998; Allen et al., 2005), numerous questions remain **open** about their population dynamics 465 in relation with **the** finescale structures.

Coupling high-resolution in-situ flow cytometry measurements performed with an adaptive and Lagrangian sampling strategy, with the size-structured population model developed by Sosik et al. (2003) allowed us to characterize the size structure of phytoplankton and to reconstruct the diurnal cycle during which cell growth and division alternate over a 24 h period in two contrasted water masses separated by a finescale front. Coupling high-resolution in-situ flow cytometry measurements in two 470 contrasted water masses with the size-structured population model developed by Sosik et al. (2003) allowed us to characterize the structure of phytoplankton and to reconstruct its diel cycle of cell growth and division on both sides of a finescale front. The values of growth rates (μ_{size}) and loss rates (l) The growth and loss rates (μ_{size} and l) found for *Synechococcus* in our study are of the same order of magnitude as **the results of** those obtained by Marrec et al. (2018), **who also applied the** size-structured model of Sosik et al. (2003) in the northwestern Mediterranean Sea using the same method. In section 3.3, we 475 **have shown** showed that the largest cells of *Synechococcus* **are dominant** were found in the older AW. These *Synechococcus* cells are characterized by a larger range of biovolume **and lower growth and loss rates**, **a lower growth rate and a higher loss rate** than those located in the younger AW (Table 2). **This is due to the fact that the older AW is composed of *Synechococcus***

480 cells transiting in all the cell cycle stages all day long (Fig. 4a–e). The cells are in average larger than in the younger AW as they grow slower at the population scale and divide less. ~~lower growth rate~~ Conversely, in the younger AW the distribution of the *Synechococcus* biovolume is narrower, which could be explained by cells ~~being~~ more active, more homogeneous in terms of size (biovolume) and better synchronized, leading to a smaller spread of the cell biovolume (Fig. 4b,d) with a dominance of ~~small~~ *Synechococcus* ~~small~~ cells (Fig. 3). ~~That explains why the patchiness of *Synechococcus* size distribution in the older AW (Fig. 4a, e) is more extensive than in the younger AW, where the size distribution is narrower (Fig. 4b, d). That~~ This also explains why higher abundances of *Synechococcus* are found in the younger AW (Fig. 3). Interestingly, the resulting net growth rate (growth minus loss) is negative in the older AW, positive in the younger AW.

485 The patchiness of size distribution of RNano and SNano (Fig. 5 and 6) is similar to those of *Synechococcus* (Fig. 4), with more extensive distribution located in the older AW, especially for SNano. As for *Synechococcus*, the nanophytoplankton patchiness could explain the distribution in terms of abundances in the two water masses (Fig. 3).

490 Results are more difficult to interpret for the nanoplankton groups RNano and SNano, expected to be mostly dominated by diatoms in the Mediterranean Sea (Marty et al., 2002; Siokou-Frangou et al., 2010; Navarro et al., 2014; El Hourany et al., 2019), especially in frontal systems (Claustre et al., 1994). RNano and SNano diel cycles are not as well-defined as for *Synechococcus*, leading to very small estimates of growth rates by the model. Optimization factors (linked to the mean squared difference between observed and predicted normalized size distributions) are relatively high and/or temporal correlations between observed and predicted mean biovolume relatively low, indicating these results must be considered with caution.

495 Nevertheless, results suggest much lower growth and loss rates for nanoplankton than for *Synechococcus* and potentially higher growth rates in the younger AW, similar to *Synechococcus* (excluding the likely unrealistic loss rate obtained for RNano in the younger AW).

500 We have also modeled the diurnal cycle for the picophytoplankton groups i.e., Pico1, Pico2, Pico3, PicoHFLR, (cf Fig. A1). However, we obtained very noisy size distributions and couldn't obtain a valid measurement, hence these distributions are not considered further in this study. A possible explanation is that picophytoplankton is often characterized by an important biodiversity (Siokou-Frangou et al., 2010) with potentially different dynamics. Indeed, except for *Synechococcus* and Cryptophytes which are taxonomic groups, the other phytoplankton groups are ataxonomic and defined only based on their size class estimated by the light scattering measured by the flow cytometer. These populations are gated out based on the expertise of the flow cytometrists. Obviously, additional analysis such as metabarcoding should have been done to address the biodiversity and test this hypothesis, but as the samples were analysed online, no sample was brought back to the laboratory to perform further investigation. On the contrary, a clear pattern was found for the nanophytoplankton group probably because the nanophytoplankton is mostly dominated by diatoms in the Mediterranean Sea (Siokou-Frangou et al., 2010), especially in frontal systems (Claustre et al., 1994). Finally, as microphytoplankton and Cryptophytes were not abundant enough to allow a reliable determination of their abundances and cell cycles, they were not considered in this study.

510 4.2 Influence of the frontal system on the phytoplankton dynamics

Oceanic finescales (typically 1–100 km) have relatively short lifetimes from days to weeks. However, due to the strong gradients created by their energetic dynamics they critically affect both ocean physics and ecology. These gradients are associated with strong vertical velocities at the origin of a vertical transport connecting the ocean's upper layer to its interior. Furthermore, the temporal scale associated with this dynamics (both horizontal and vertical) is in the same order of magnitude than many
515 important oceanic processes including biogeochemical cycles and biodiversity. This suggests the possibility of a close coupling between the finescale forcing and the phytoplankton distribution and growth. Our previous article Tzortzis et al., 2021 provided a description of the hydrodynamics and the hydrology of the region, in the same of the area of the present of the region South of the Balearic Islands corresponding to a cross-over of the next SWOT satellite (Fig. 1). In the following, we attempt to establish the potential link between these different physical forcings and the particular distribution of phytoplankton in terms of cells
520 size and abundances. Figure 7 summarizes the physical forcing evidenced in this area in the previous publication during the PROTEVS MED-SWOT cruise, superimposed with the biovolumes and the abundances of the different phytoplankton groups sampled *in situ* by the automated flow cytometer.

Physical hydrodynamics and, in particular, vertical velocities play a key role on phytoplankton dynamics as vertical velocities modulate nutrients availability and irradiance of phytoplankton (intensity and quality vary with depth), two essential variables
525 for phytoplankton growth (Lévy et al., 2001; Pidcock et al., 2016; Mahadevan, 2016). The computation of the vertical motions in the frontal area, as represented in Fig. 7 (see also Fig. A3), show the presence of upwellings and downwellings in the frontal area. The older AW is characterized by larger cells of *Synechococcus* and nanophytoplankton with low abundances, low intrinsic growth rates and negative net growth rates, suggesting an older, declining population, whereas the younger AW is dominated by small cells with high abundances, and at least for *Synechococcus* high intrinsic growth rates and a positive
530 net growth rate, suggesting a slightly growing or stable population (nanoplankton results in the younger AW are subject to caution as optimization factors are relatively high). Furthermore, microphytoplankton (i.e. largest type of phytoplankton) is more abundant in older AW than in the younger AW. A possible explanation is that these two water masses are characterized by different nutrient concentrations, thus favoring certain phytoplankton groups. Bethoux (1989) and Schroeder et al. (2010) have observed that the older AW is slightly more enriched with nutrients than the younger because the older AW receives nutrient
535 inputs from the continent (river discharges, rain, wind) during its circulation across the Mediterranean basin. Unfortunately, it was not possible for both technical and funding reasons to perform nutrient measurements during the 2018 cruise, so that we cannot conclusively assess nutrient patterns during the cruise. Assuming that the nutrient distribution across the two water masses was similar to what was previously measured by Bethoux (1989) and Schroeder et al. (2010), we propose that higher nutrient concentrations in the older AW explain the observed phytoplankton cell size and abundances distributions. Our
540 hypothesis is supported by similar observations by Jacquet et al. (2010) and Mena et al. (2016) who also found the highest abundances of the small phytoplankton (*Synechococcus* and picophytoplankton) in the most oligotrophic waters, i.e., the younger AW. Furthermore, previous studies have shown that the proportion of picophytoplankton in the total phytoplankton biomass is higher in oligotrophic regions than in mesotrophic or eutrophic regions (Zhang et al., 2008; Zhang et al., 2012).

Indeed, their better surface: size ratio due to their small size confers them a better capacity to inhabit areas with very low
545 nutrient concentration compared to larger phytoplankton (Kiørboe, 1993; Marañón, 2015). Since our study area is always oligotrophic (Moutin et al., 2012), a small variation of the nutrient concentration (typically $\leq 0.1 \mu\text{M}$ of nitrate) is sufficient to generate higher abundance of picophytoplankton. Some studies have attempted to highlight a link between hydrological condition and the phytoplankton dynamic (Qasim et al., 1972 ; Brunet et al., 2006 ; Marañón et al., 2012, e.g.). However, their results showed that the influence of these hydrological parameters on the phytoplankton growth and distribution was difficult
550 to estimate, compared to the effects of nutrient availability and radiation exposure.

Our previous article (Tzortzis et al., 2021) provided a description of the hydrodynamics and the hydrology of the region. In the following, we attempt to establish the potential link between the characteristics of the two AW separated by the front, the physical forcings associated with this frontal structure and the particular distribution of phytoplankton in terms of cells size
555 and abundances. Figure 7 summarizes the physical forcing evidenced in this frontal area in the previous publication during the PROTEVSMED-SWOT cruise, superimposed with the biovolumes and the abundances of the different phytoplankton groups sampled in situ by the automated flow cytometer.

The older AW is characterized by larger cells of *Synechococcus* and nanophytoplankton with low abundances, low intrinsic growth rates and negative net growth rates, suggesting an older, declining population, whereas the younger AW is dominated
560 by small cells with high abundances, and at least for *Synechococcus* high intrinsic growth rates and a positive net growth rate, suggesting a slightly growing or stable population (nanoplankton results in the younger AW are subject to caution as optimization factors are relatively high). Furthermore, microphytoplankton (i.e largest type of phytoplankton) is more abundant in older AW than in the younger AW. The early experimental works of Marshall and Orr (1928); Jenkin (1937); Huisman (1999)
565 have well established that the light and nutrients are essential for phytoplankton growth. The reconstruction of the circadian cycle indicates that irradiance was similar in the two water masses (Fig. 4, 5 and 6, red lines), with corresponding daily total irradiance of 286 and $299 \mu\text{E m}^{-2}$ for the older AW and the younger AW, respectively (Fig. A2). That is why, the availability
570 of light seems not to be the principal cause explaining the difference of phytoplankton dynamics and its distribution in the two AW. An other possible explanation is that these two water masses are characterized by different nutrient concentrations, thus favoring certain phytoplankton groups. Bethoux (1989) and Schroeder et al. (2010) have observed that the older AW is slightly more enriched with nutrients than the younger AW because the older AW receives nutrient inputs from the continent
575 (river discharges, rain, wind) during its circulation across the Mediterranean basin. Unfortunately, it was not possible for both technical and funding reasons to perform nutrient measurements during the 2018 cruise, so that we cannot conclusively assess nutrient patterns during the cruise. Assuming that the nutrient distribution across the two water masses was similar to what was previously measured by Bethoux (1989) and Schroeder et al. (2010), we propose that higher nutrient concentrations in the older AW explain the observed phytoplankton cell size and abundances distributions. Our hypothesis is supported by similar observations by Jacquet et al. (2010) and Mena et al. (2016) who also found the highest abundances of the small phytoplankton (*Synechococcus* and picophytoplankton) in the most oligotrophic waters, i.e., the younger AW. Furthermore, previous studies have shown that the proportion of picophytoplankton in the total phytoplankton biomass is higher in oligotrophic regions than

in mesotrophic or eutrophic regions (Zhang et al., 2008; Cerino et al., 2012). Indeed, their better surface:size ratio due to their
580 small size confers them a better capacity to inhabit areas with very low nutrient concentration compared to larger phytoplankton (Kiørboe, 1993; Marañón, 2015). Since our study area is always oligotrophic (Moutin et al., 2012), a small variation of the nutrient concentration (typically $\leq 0.1 \mu\text{M}$ of nitrate) is sufficient to generate higher abundance of picophytoplankton. Some studies have attempted to link hydrological condition and the phytoplankton dynamic (Qasim et al., 1972; Brunet et al., 2006; Marañón et al., 2012, e.g.). However, their results showed that the influence of these hydrological parameters on the
585 phytoplankton growth and distribution was difficult to estimate, compared to the effects of nutrient availability and radiation exposure.

Other physical processes occurring at the front can explain the different dynamics of phytoplankton groups. The work of Lévy et al. (2001); Pidcock et al. (2016); Mahadevan (2016) have highlighted that the availability of light and nutrient is driven by physical dynamics such as vertical velocities. The computation of the vertical motions in the frontal area, as represented in
590 Fig. 7 (see also Fig. A3), show the presence of upwellings and downwellings in the frontal area. However, due to the lack of nutrients measurements during the cruise, we are not able to quantify the impact of these vertical velocities.

5 Conclusion and perspectives

~~Phytoplankton structure and dynamics are a complex result of many interacting biological and physical phenomena. Biological processes can be either intrinsic, such as cell growth, or extrinsic such as cell death by viral lysis or grazing. Physical forcings in particular at finescales are also important, because they can influence the nutrient and irradiance, both parameters being fundamental for primary production by photosynthesis.~~

~~In this study, we have focused on a frontal structure separating two distinct water masses both in terms of hydrology and phytoplankton abundances. The reconstruction of the diurnal cycle for several phytoplankton groups in these two water masses, under the influence of physical conditions met in situ provides a better understanding of the particular distribution of the phytoplankton groups in this area. The estimates of specific growth rates for the various phytoplankton groups is a key to better understand and quantify their respective biogeochemical and ecological contributions in oligotrophic ecosystems, where they play a major role. Furthermore, direct integration of growth rates in biogeochemical models (Cullen et al., 1993) should be taken into account for a better assessment of the biogeochemical contribution of phytoplankton in oligotrophic ecosystems and to better forecast its evolution in the context of global change.~~

~~This work paves the way for the future cruise which will provide a unique opportunity for a more detailed study of physical-biological finescale coupling. Indeed, we plan future experiments again in the South-western Mediterranean in spring 2023, after the launch of the SWOT satellite which will provide high-resolution altimetry-derived current. Involving high-resolution nutrient measurements (and also high-precision ones, considering the oligotrophy of the Mediterranean Sea), coupled with metabarcoding (to address the biodiversity of phytoplankton), zooplankton and virus sampling, we will improve the understanding of zooplankton grazing and viral lysis on the different phytoplankton groups. Furthermore, we aim to explore how biogeochemical and ecological role of the finescales in regions of weak circulation are different from the ones more~~

documented in highly energetic regions like boundary currents. In the Mediterranean sea, the low nutrient content is indeed the perfect condition when addressing this question, because even weak horizontal or vertical nutrient redistributions associated with the finescale circulation are likely to result in a biological response (Talmy et al., 2014; Hashihama et al., 2021).

615

Phytoplankton structure and dynamics are a complex result of many interacting biological and physical phenomena. Finescale structures, and in particular fronts, generate vertical velocities which displace phytoplankton cells and nutrients in the water column, thus influencing phytoplankton communities. These mechanisms are only partially understood because the spatial scale of these structures and their ephemeral nature make them particularly difficult to study in situ; as a consequence only 620 a few studies have been performed in finescale frontal regions. The estimates of specific growth rates for the various phytoplankton groups is one of the keys to better understand how environmental conditions affect phytoplankton dynamics. In this study, we followed the dynamics of several phytoplankton groups in two distinct water masses both in terms of hydrology and phytoplankton abundances, in order to explain their particular distribution.

The originality of our work resides in the fact that we used a size-structured population model applied in two water masses 625 identified using a Lagrangian sampling strategy. To our knowledge this had never been done before. This strategy allowed us to reconstruct the diurnal cycle of several phytoplankton groups and to identify contrasted dynamics in the two water masses. For *Synechococcus* and nanophytoplankton, we found higher cell size in the older AW located north of the front, associated with lower abundances. A possible explanation is that the older AW is more enriched in nutrients than the younger AW, thus favoring larger cells. This remains a hypothesis because of a lack of nutrient data. Another novelty of our study is that we 630 applied the Sosik et al. (2003) model on several phytoplankton groups identified by flow cytometry, whereas previous studies only applied it to *Synechococcus* and *Prochlorococcus* (Ribalet et al., 2010; Hunter-Cevera et al., 2014; Marrec et al., 2018; Fowler et al., 2020) or to certain types of diatoms (Dugenne et al., 2014). We obtained good results for *Synechococcus* and nanophytoplankton. However, our results were noisy for picophytoplankton groups probably because they contain several taxa with differing dynamics (Siokou-Frangou et al., 2010; Le Moal et al., 2011).

635 Our work paves the way for many research perspectives. Direct integration of growth rates in biogeochemical models (Cullen et al., 1993) should be taken into account for a better assessment of the biogeochemical contribution of phytoplankton in oligotrophic ecosystems and to better forecast its evolution in the context of global change. Furthermore, we plan future experiments again in the South Western Mediterranean in spring 2023, during the fast-sampling phase of the SWOT satellite mission 640 (necessary considering the oligotrophy of the Mediterranean Sea), coupled with DNA metabarcoding (to address phytoplankton biodiversity), zooplankton and virus sampling, we will improve the understanding of zooplankton grazing and viral lysis on the different phytoplankton groups. Furthermore, we aim to explore how the biogeochemical and ecological role of finescale structures in regions of weak circulation differ from those documented in highly energetic regions like boundary currents. In the Mediterranean sea, the low nutrient content is indeed the perfect condition when addressing this question, because even 645 weak horizontal or vertical nutrient redistributions associated with the finescale circulation are likely to result in a biological response (Talmy et al., 2014; Hashihama et al., 2021).

Data availability. The physical data are open access and available at <https://www.seanoe.org/data/00512/62352/> (last access: April 22, 2023) (Dumas, 2018). Flow cytometry data are available by request to the corresponding author.

Author contributions. RT post-processed the in situ observations, performed the analysis of the results and led the writing of the manuscript.
650 AD and GG designed the Lagrangian experiment and collected the in situ data together with FD. AP, SB and FdO provided land support concerning the sampling strategy. LI carried out the analysis of flow cytometry data. MM and YZ provided their expertise about the flow cytometry analysis and the results obtained with the size-structured population model. All the authors discussed the results and contributed to the writing of the manuscript.

Competing interests. The contact author has declared that neither they nor their co-authors have any competing interests.

655 *Acknowledgements.* This work was supported by the CNES in the framework of the BIOSWOT-AdAC project (<https://www.swot-adac.org/>, last access: April 22, 2023) by the MIO Axes Transverses program (AT-COUPAGE) and the Sino-French IRP (CNRS-CAS) DYF2M program. The chlorophyll *a* product is produced by CLS. The authors thank the SHOM and the crew of the RV *Beautemps-Beaupré* for shipboard operations. The authors thank also Melilotus Thyssen for providing the CytoBuoy® flow cytometer and her help in flow cytometry data analysis. The flow cytometer was funded by the CHROME project, Excellence Initiative of Aix-Marseille University – A*MIDEX, a
660 French 11 Investissements d’Avenir program. SPASSO is operated and developed with the support of the SIP (Service Informatique de Pythéas) and in particular Christophe Yohia, Julien Lecubin, Didier Zevaco and Cyrille Blanpain (Institut Pythéas, Marseille, France). The project leading to this publication received funding from the European FEDER Fund under project number 1166-39417. Roxane Tzortzis is financed by a MENRT PhD grant (École Doctorale Sciences de l’environnement – ED 251, Aix-Marseille University).

References

- 665 Allen, J. T., Brown, L., Sanders, R., Mark Moore, C., Mustard, A., Fielding, S., Lucas, M., Rixen, M., Savidge, G., Henson, S., et al.: Diatom carbon export enhanced by silicate upwelling in the northeast Atlantic, *Nature*, 437, 728–732, <https://doi.org/10.1038/nature03948>, 2005.
- Balbín, R., Flexas, M. d. M., López-Jurado, J. L., Peña, M., Amores, A., and Alemany, F.: Vertical velocities and biological consequences at a front detected at the Balearic Sea, *Cont. Shelf. Res.*, 47, 28–41, <https://doi.org/10.1016/j.csr.2012.06.008>, 2012.
- Balbín, R., López-Jurado, J. L., Flexas, M., Reglero, P., Vélez-Velchí, P., González-Pola, C., Rodríguez, J. M., García, A., and Alemany, F.: Interannual variability of the early summer circulation around the Balearic Islands: driving factors and potential effects on the marine ecosystem, *J. Marine Syst.*, 138, 70–81, <https://doi.org/10.1016/j.jmarsys.2013.07.004>, 2014.
- 670 Barceló-Llull, B., Pascual, A., Ruiz, S., Escudier, R., Torner, M., and Tintoré, J.: Temporal and spatial hydrodynamic variability in the Mallorca channel (western Mediterranean Sea) from 8 years of underwater glider data, *J. Geophys. Res.-Oceans*, 124, 2769–2786, <https://doi.org/10.1029/2018JC014636>, 2019.
- 675 Bethoux, J.: Oxygen consumption, new production, vertical advection and environmental evolution in the Mediterranean Sea, *Deep-Sea Res.*, 36, 769–781, [https://doi.org/10.1016/0198-0149\(89\)90150-7](https://doi.org/10.1016/0198-0149(89)90150-7), 1989.
- Boyd, P. and Newton, P.: Does planktonic community structure determine downward particulate organic carbon flux in different oceanic provinces?, *Deep-Sea Res. Pt I*, 46, 63–91, [https://doi.org/10.1016/S0967-0637\(98\)00066-1](https://doi.org/10.1016/S0967-0637(98)00066-1), 1999.
- 680 Brunet, C., Casotti, R., Vantrepotte, V., Corato, F., and Conversano, F.: Picophytoplankton diversity and photoacclimation in the Strait of Sicily (Mediterranean Sea) in summer. I. Mesoscale variations, *Aquat. Microb. Ecol.*, 44, 127–141, <https://doi.org/10.3354/ame044127>, 2006.
- Capet, X., McWilliams, J. C., Molemaker, M. J., and Shchepetkin, A.: Mesoscale to submesoscale transition in the California Current System. Part II: Frontal processes, *J. Phys. Oceanogr.*, 38, 44–64, <https://doi.org/10.1175/2007JPO3672.1>, 2008a.
- 685 Capet, X., Mcwilliams, J. C., Molemaker, M. J., and Shchepetkin, A. F.: Mesoscale to submesoscale transition in the California Current System. Part I: Flow structure, eddy flux, and observational tests, *J. Phys. Oceanogr.*, 38, 29–43, <https://doi.org/10.1175/2007JPO3671.1>, 2008b.
- Cerino, F., Aubry, F. B., Coppola, J., La Ferla, R., Maimone, G., Socal, G., and Totti, C.: Spatial and temporal variability of pico-, nano-and microphytoplankton in the offshore waters of the southern Adriatic Sea (Mediterranean Sea), *Cont. Shelf Res.*, 44, 94–105, <https://doi.org/10.1016/j.csr.2011.06.006>, 2012.
- 690 Claustre, H., Kerhervé, P., Marty, J. C., Prieur, L., Videau, C., and Hecq, J.-H.: Phytoplankton dynamics associated with a geostrophic front: ecological and biogeochemical implications, *J. Mar. Res.*, 52, 711–742, <https://doi.org/10.1357/0022240943077000>, 1994.
- Clayton, S., Nagai, T., and Follows, M. J.: Fine scale phytoplankton community structure across the Kuroshio Front, *J. Plankton. Res.*, 36, 1017–1030, <https://doi.org/10.1093/plankt/fbu020>, 2014.
- 695 Clayton, S., Lin, Y.-C., Follows, M. J., and Worden, A. Z.: Co-existence of distinct Ostreococcus ecotypes at an oceanic front, *Limnol. Oceanogr.*, 62, 75–88, <https://doi.org/10.1002/lno.10373>, 2017.
- Cotroneo, Y., Aulicino, G., Ruiz, S., Pascual, A., Budillon, G., Fusco, G., and Tintoré, J.: Glider and satellite high resolution monitoring of a mesoscale eddy in the algerian basin: Effects on the mixed layer depth and biochemistry, *J. Marine Syst.*, 162, 73–88, <https://doi.org/10.1016/j.jmarsys.2015.12.004>, 2016.

- Cullen, J. J., Geider, R., Ishizaka, J., Kiefer, D., Marra, J., Sakshaug, E., and Raven, J.: Towards a general description of phytoplankton
700 growth for biogeochemical models, in: Towards a model of ocean biogeochemical processes, pp. 153–176, Springer, Berlin, Heidelberg,
https://doi.org/10.1007/978-3-642-84602-1_7, 1993.
- De La Rocha, C. L. and Passow, U.: Factors influencing the sinking of POC and the efficiency of the biological carbon pump, *Deep-Sea Res. Pt. II*, 54, 639–658, <https://doi.org/10.1016/j.dsr2.2007.01.004>, 2007.
- Dubelaar, G. and Gerritzen, P.: CytoBuoy: a step forward towards using flow cytometry in operational oceanography, *Sci. Mar.*, 64, 255–265,
705 <https://doi.org/10.3989/scimar.2000.64n2255>, 2000.
- Dubelaar, G. B. and Jonker, R. R.: Flow cytometry as a tool for the study of phytoplankton, *Sci. Mar.*, 64, 135–156,
<https://doi.org/10.3989/scimar.2000.64n2135>, 2000.
- Dubelaar, G. B., Gerritzen, P. L., Beeker, A. E., Jonker, R. R., and Tangen, K.: Design and first results of CytoBuoy: A wireless flow cytometer
710 for in situ analysis of marine and fresh waters, *Cytometry: The Journal of the International Society for Analytical Cytology*, 37, 247–254,
[https://doi.org/10.1002/\(SICI\)1097-0320\(19991201\)37:4<247::AID-CYTO1>3.0.CO;2-9](https://doi.org/10.1002/(SICI)1097-0320(19991201)37:4<247::AID-CYTO1>3.0.CO;2-9), 1999.
- Dugenne, M., Thyssen, M., Nerini, D., Mante, C., Poggiale, J.-C., Garcia, N., Garcia, F., and Grégori, G. J.: Consequence of a sudden wind
event on the dynamics of a coastal phytoplankton community: an insight into specific population growth rates using a single cell high
frequency approach, *Front. Microbiol.*, 5, 485, <https://doi.org/10.3389/fmicb.2014.00485>, 2014.
- Dumas, F.: PROTEVSMED_SWOT_2018_LEG1 cruise, RV Beautemps-Beaupré, https://doi.org/10.17183/protevsmed_swot_2018_leg1,
715 2018.
- Edwards, K. F., Thomas, M. K., Klausmeier, C. A., and Litchman, E.: Light and growth in marine phytoplankton: allometric, taxonomic, and
environmental variation, *Limnol. Oceanogr.*, 60, 540–552, <https://doi.org/10.1002/lno.10033>, 2015.
- El Hourany, R., Abboud-abi Saab, M., Faour, G., Mejia, C., Crépon, M., and Thiria, S.: Phytoplankton diversity in the Mediterranean Sea
from satellite data using self-organizing maps, *J. Geophys. Res.-Oceans*, 124, 5827–5843, <https://doi.org/10.1029/2019JC015131>, 2019.
- 720 Field, C. B., Behrenfeld, M. J., Randerson, J. T., and Falkowski, P.: Primary production of the biosphere: integrating terrestrial and oceanic
components, *Science*, 281, 237–240, <https://doi.org/10.1126/science.281.5374.237>, 1998.
- Foladori, P., Quaranta, A., and Ziglio, G.: Use of silica microspheres having refractive index similar to bacteria for conversion of flow
cytometric forward light scatter into biovolume, *Water Res.*, 42, 3757–3766, <https://doi.org/10.1016/j.watres.2008.06.026>, 2008.
- Fontana, S., Thomas, M. K., Moldoveanu, M., Spaak, P., and Pomati, F.: Individual-level trait diversity predicts phytoplankton community
725 properties better than species richness or evenness, *The ISME journal*, 12, 356–366, <https://doi.org/10.1038/ismej.2017.160>, 2018.
- Fowler, B. L., Neubert, M. G., Hunter-Cevera, K. R., Olson, R. J., Shalapyonok, A., Solow, A. R., and Sosik, H. M.: Dynamics
and functional diversity of the smallest phytoplankton on the Northeast US Shelf, *P. Natl. Acad. Sci.*, 117, 12 215–12 221,
<https://doi.org/10.1073/pnas.1918439117>, 2020.
- Garreau, P., Dumas, F., Louazel, S., Correard, S., Fercocq, S., Le Menn, M., Serpette, A., Garnier, V., Stegner, A., Le Vu, B., et al.: PROTEVSMED
730 field experiments: very high resolution hydrographic surveys in the Western Mediterranean Sea, *Earth. Syst. Sci. Data*, 12, 441–456,
<https://doi.org/10.5194/essd-12-441-2020>, 2020.
- Gaube, P., Chelton, D. B., Samelson, R. M., Schlax, M. G., and O'Neill, L. W.: Satellite observations of mesoscale eddy-induced Ekman
pumping, *J. Phys. Oceanogr.*, 45, 104–132, <https://doi.org/10.1175/JPO-D-14-0032.1>, 2015.
- Geider, R., MacIntyre, H., and Kana, T.: Dynamic model of phytoplankton growth and acclimation: responses of the balanced
735 growth rate and the chlorophyll a: carbon ratio to light, nutrient-limitation and temperature, *Mar. Ecol. Prog. Ser.*, 148, 187–200,
<https://doi.org/10.3354/meps148187>, 1997.

- Geyer, C. J.: Practical markov chain monte carlo, *Stat. Sci.*, pp. 473–483, 1992.
- Giordani, H., Prieur, L., and Caniaux, G.: Advanced insights into sources of vertical velocity in the ocean, *Ocean Dynam.*, 56, 513–524, <https://doi.org/10.1007/s10236-005-0050-1>, 2006.
- 740 Guidi, L., Stemmann, L., Jackson, G. A., Ibanez, F., Claustre, H., Legendre, L., Picheral, M., and Gorsky, G.: Effects of phytoplankton community on production, size, and export of large aggregates: A world-ocean analysis, *Limnol. Oceanogr.*, 54, 1951–1963, <https://doi.org/10.4319/lo.2009.54.6.1951>, 2009.
- Hashihama, F., Saito, H., Kodama, T., Yasui-Tamura, S., Kanda, J., Tanita, I., Ogawa, H., Woodward, E. M. S., Boyd, P. W., and Furuya, K.: Cross-basin differences in the nutrient assimilation characteristics of induced phytoplankton blooms in the subtropical Pacific waters, *Biogeosciences*, 18, 897–915, <https://doi.org/10.5194/bg-18-897-2021>, 2021.
- 745 Hilligesøe, K. M., Richardson, K., Bendtsen, J., Sørensen, L.-L., Nielsen, T. G., and Lyngsgaard, M. M.: Linking phytoplankton community size composition with temperature, plankton food web structure and sea–air CO₂ flux, *Deep-Sea Res. Pt I*, 58, 826–838, <https://doi.org/10.1016/j.dsr.2011.06.004>, 2011.
- Huisman, J.: Population dynamics of light-limited phytoplankton: microcosm experiments, *Ecology*, 80, 202–210, [https://doi.org/10.1890/0012-9658\(1999\)080\[0202:PDOLLP\]2.0.CO;2](https://doi.org/10.1890/0012-9658(1999)080[0202:PDOLLP]2.0.CO;2), 1999.
- 750 Hunter-Cevera, K. R., Neubert, M. G., Solow, A. R., Olson, R. J., Shalapyonok, A., and Sosik, H. M.: Diel size distributions reveal seasonal growth dynamics of a coastal phytoplankton, *P. Natl. Acad. Sci. USA*, 111, 9852–9857, <https://doi.org/10.1073/pnas.1321421111>, 2014.
- Jacquet, S., Prieur, L., Nival, P., and Vaultot, D.: Structure and variability of the microbial community associated to the Alboran Sea frontal system (Western Mediterranean) in winter, *J. Oceanogr. Research and data*, 3, 47–75, <https://hal.inrae.fr/hal-02656403>, 2010.
- 755 Jenkin, P. M.: Oxygen production by the diatom *Coscinodiscus excentricus* Ehr. in relation to submarine illumination in the English Channel, *J. Mar. Biol. Assoc. UK*, 22, 301–343, <https://doi.org/10.1017/S0025315400012030>, 1937.
- Kiørboe, T.: Turbulence, phytoplankton cell size, and the structure of pelagic food webs, in: *Adv. Mar. Biol.*, vol. 29, pp. 1–72, Elsevier, [https://doi.org/10.1016/S0065-2881\(08\)60129-7](https://doi.org/10.1016/S0065-2881(08)60129-7), 1993.
- Koch, A. L., Robertson, B. R., and Button, D. K.: Deduction of the cell volume and mass from forward scatter intensity of bacteria analyzed by flow cytometry, *J. Microbiol. Meth.*, 27, 49–61, [https://doi.org/10.1016/0167-7012\(96\)00928-1](https://doi.org/10.1016/0167-7012(96)00928-1), 1996.
- 760 Le Moal, M., Collin, H., and Biegala, I. C.: Intriguing diversity among diazotrophic picoplankton along a Mediterranean transect: a dominance of rhizobia, *Biogeosciences*, 8, 827–840, <https://doi.org/10.5194/bg-8-827-2011>, 2011.
- Lévy, M., Klein, P., and Treguier, A.-M.: Impact of sub-mesoscale physics on production and subduction of phytoplankton in an oligotrophic regime, *J. Mar. Res.*, 59, 535–565, <https://doi.org/10.1357/002224001762842181>, 2001.
- 765 Lévy, M., Franks, P., and Smith, K.: The role of submesoscale currents in structuring marine ecosystems, *Nat. Commun.*, 9, 4758, <https://doi.org/10.1038/s41467-018-07059-3>, 2018.
- MacIntyre, H. L., Kana, T. M., and Geider, R. J.: The effect of water motion on short-term rates of photosynthesis by marine phytoplankton, *Trends Plant Sci.*, 5, 12–17, [https://doi.org/10.1016/S1360-1385\(99\)01504-6](https://doi.org/10.1016/S1360-1385(99)01504-6), 2000.
- Mahadevan, A.: The impact of submesoscale physics on primary productivity of plankton, *Annu. Rev. Mar. Sci.*, 8, 161–184, <https://doi.org/10.1146/annurev-marine-010814-015912>, 2016.
- 770 Mahadevan, A. and Tandon, A.: An analysis of mechanisms for submesoscale vertical motion at ocean fronts, *Ocean Model.*, 14, 241–256, <https://doi.org/10.1016/j.ocemod.2006.05.006>, 2006.
- Marañón, E.: Cell size as a key determinant of phytoplankton metabolism and community structure, *Annu. Rev. Mar. Sci.*, 7, 241–264, <https://doi.org/10.1146/annurev-marine-010814-015955>, 2015.

- 775 Marañón, E., Cermeno, P., Latasa, M., and Tadonléké, R. D.: Temperature, resources, and phytoplankton size structure in the ocean, *Limnol. Oceanogr.*, 57, 1266–1278, <https://doi.org/10.4319/lo.2012.57.5.1266>, 2012.
- Marrec, P., Grégori, G., Doglioli, A. M., Dugenne, M., Della Penna, A., Bhairy, N., Cariou, T., Hélias Nunige, S., Lahbib, S., Rougier, G., Wagener, T., and Thyssen, M.: Coupling physics and biogeochemistry thanks to high-resolution observations of the phytoplankton community structure in the northwestern Mediterranean Sea, *Biogeosciences*, 15, 1579–1606, <https://doi.org/10.5194/bg-15-1579-2018>, 780 2018.
- Marshall, S. M. and Orr, A.: The photosynthesis of diatom cultures in the sea, *J. Mar. Biol. Assoc. UK*, 15, 321–360, <https://doi.org/10.1017/S0025315400055703>, 1928.
- Martin, A. P. and Richards, K. J.: Mechanisms for vertical nutrient transport within a North Atlantic mesoscale eddy, *Deep-Sea Res. Pt II*, 48, 757–773, [https://doi.org/10.1016/S0967-0645\(00\)00096-5](https://doi.org/10.1016/S0967-0645(00)00096-5), 2001.
- 785 Marty, J.-C., Chiavérini, J., Pizay, M.-D., and Avril, B.: Seasonal and interannual dynamics of nutrients and phytoplankton pigments in the western Mediterranean Sea at the DYFAMED time-series station (1991–1999), *Deep-Sea Res. Pt II*, 49, 1965–1985, [https://doi.org/10.1016/S0967-0645\(02\)00022-X](https://doi.org/10.1016/S0967-0645(02)00022-X), 2002.
- McDougall, T., Jackett, D., Millero, F., Pawlowicz, R., and Barker, P.: A global algorithm for estimating Absolute Salinity., *Ocean Sci.*, 8, 1123–1134, <https://doi.org/10.5194/os-8-1123-2012>, 2012.
- 790 McGillicuddy Jr, D. J.: Mechanisms of physical-biological-biogeochemical interaction at the oceanic mesoscale, *Annu. Rev. Mar. Sci.*, 8, 125–159, <https://doi.org/10.1146/annurev-marine-010814-015606>, 2016.
- McGillicuddy Jr, D. J., Robinson, A., Siegel, D., Jannasch, H., Johnson, R., Dickey, T., McNeil, J., Michaels, A., and Knap, A.: Influence of mesoscale eddies on new production in the Sargasso Sea, *Nature*, 394, 263–266, <https://doi.org/10.1038/28367>, 1998.
- 795 McGillicuddy Jr, D. J., Anderson, L. A., Bates, N. R., Bibby, T., Buesseler, K. O., Carlson, C. A., Davis, C. S., Ewart, C., Falkowski, P. G., Goldthwait, S. A., et al.: Eddy/wind interactions stimulate extraordinary mid-ocean plankton blooms, *Science*, 316, 1021–1026, <https://doi.org/10.1126/science.1136256>, 2007.
- McWilliams, J. C.: Submesoscale currents in the ocean, *P. Roy. Soc. A-Math. Phys.*, 472, 20160 117, <https://doi.org/10.1098/rspa.2016.0117>, 2016.
- Mena, C., Reglero, P., Ferriol, P., Torres, A. P., Aparicio-González, A., Balbín, R., Santiago, R., Moyà, G., Alemany, F., and Agawin, N. S.: 800 Prokaryotic picoplankton spatial distribution during summer in a haline front in the Balearic Sea, Western Mediterranean, *Hydrobiologia*, 779, 243–257, <https://doi.org/10.1007/s10750-016-2825-4>, 2016.
- Millot, C.: Circulation in the western Mediterranean Sea, *J. Marine Syst.*, 20, 423–442, [https://doi.org/10.1016/S0924-7963\(98\)00078-5](https://doi.org/10.1016/S0924-7963(98)00078-5), 1999.
- Millot, C. and Taupier-Letage, I.: Circulation in the Mediterranean Sea, in: *The Mediterranean Sea*, edited by Saliot, A., pp. 29–66, Springer, 805 Berlin, Heidelberg, Germany, <https://doi.org/10.1007/b107143>, 2005.
- Millot, C., Candela, J., Fuda, J.-L., and Tber, Y.: Large warming and salinification of the Mediterranean outflow due to changes in its composition, *Deep-Sea Res. Pt. I*, 53, 656–666, <https://doi.org/10.1016/j.dsr.2005.12.017>, 2006.
- Moutin, T., Van Wambeke, F., and Prieur, L.: Introduction to the Biogeochemistry from the Oligotrophic to the Ultraoligotrophic Mediterranean (BOUM) experiment, *Biogeosciences*, 9, 3817–3825, <https://doi.org/10.5194/bg-9-3817-2012>, 2012.
- 810 Mouw, C. B., Barnett, A., McKinley, G. A., Gloege, L., and Pilcher, D.: Phytoplankton size impact on export flux in the global ocean, *Global Biogeochem. Cy.*, 30, 1542–1562, <https://doi.org/10.1002/2015GB005355>, 2016.

- Navarro, G., Alvain, S., Vantrepotte, V., and Huertas, I. E.: Identification of dominant phytoplankton functional types in the Mediterranean Sea based on a regionalized remote sensing approach, *Remote Sens. Environ.*, 152, 557–575, <https://doi.org/10.1016/j.rse.2014.06.029>, 2014.
- 815 Neal, R. M.: Probabilistic inference using Markov chain Monte Carlo methods, Department of Computer Science, University of Toronto Toronto, ON, Canada, 1993.
- Pascual, A., Ruiz, S., Olita, A., Troupin, C., Claret, M., Casas, B., Mourre, B., Poulain, P.-M., Tovar-Sanchez, A., Capet, A., et al.: A multiplatform experiment to unravel meso-and submesoscale processes in an intense front (AlborEx), *Front. Mar. Sci.*, 4, 39, <https://doi.org/10.3389/fmars.2017.00039>, 2017.
- 820 Petrenko, A. A., Doglioli, A. M., Nencioli, F., Kersalé, M., Hu, Z., and d’Ovidio, F.: A review of the LATEX project: mesoscale to submesoscale processes in a coastal environment, *Ocean Dynam.*, 67, 513–533, <https://doi.org/10.1007/s10236-017-1040-9>, 2017.
- Pidcock, R. E., Martin, A. P., Painter, S. C., Allen, J. T., Srokosz, M. A., Forryan, A., Stinchcombe, M., and Smeed, D. A.: Quantifying mesoscale-driven nitrate supply: A case study, *Global Biogeochem. Cy.*, 30, 1206–1223, <https://doi.org/10.1002/2016GB005383>, 2016.
- Pilo, G. S., Oke, P. R., Coleman, R., Rykova, T., and Ridgway, K.: Patterns of vertical velocity induced by eddy distortion in an ocean model, 825 *J. Geophys. Res.-Oceans*, 123, 2274–2292, <https://doi.org/10.1002/2017JC013298>, 2018.
- Qasim, S., Bhattachari, P., and Devassy, V.: The influence of salinity on the rate of photosynthesis and abundance of some tropical phytoplankton, *Mar. Biol.*, 12, 200–206, <https://doi.org/10.1007/BF00346767>, 1972.
- Reynolds, C. S.: *The ecology of phytoplankton*, Cambridge University Press, 2006.
- Ribalet, F., Marchetti, A., Hubbard, K. A., Brown, K., Durkin, C. A., Morales, R., Robert, M., Swalwell, J. E., Tortell, P. D., and Armbrust, 830 E. V.: Unveiling a phytoplankton hotspot at a narrow boundary between coastal and offshore waters, *Proc. Nat. Acad. Sci. USA*, 107, 16 571–16 576, <https://doi.org/10.1073/pnas.1005638107>, 2010.
- Schroeder, K., Gasparini, G., Borghini, M., Cerrati, G., and Delfanti, R.: Biogeochemical tracers and fluxes in the Western Mediterranean Sea, spring 2005, *J. Marine Syst.*, 80, 8–24, <https://doi.org/10.1016/j.jmarsys.2009.08.002>, 2010.
- 835 Shcherbina, A. Y., Sundermeyer, M. A., Kunze, E., D’Asaro, E., Badin, G., Birch, D., Brunner-Suzuki, A.-M. E., Callies, J., Kuebel Cervantes, B. T., Claret, M., et al.: The LatMix summer campaign: Submesoscale stirring in the upper ocean, *Bull. Amer. Meteorol. Soc.*, 96, 1257–1279, <https://doi.org/10.1175/BAMS-D-14-00015.1>, 2015.
- Sieburth, J. M., Smetacek, V., and Lenz, J.: Pelagic ecosystem structure: Heterotrophic compartments of the plankton and their relationship to plankton size fractions, *Limnol. Oceanogr.*, 23, 1256–1263, <https://doi.org/10.4319/lo.1978.23.6.1256>, 1978.
- 840 Siokou-Frangou, I., Christaki, U., Mazzocchi, M. G., Montresor, M., Ribera d’Alcalá, M., Vaqué, D., and Zingone, A.: Plankton in the open Mediterranean Sea: a review, *Biogeosciences*, 7, 1543–1586, <https://doi.org/10.5194/bg-7-1543-2010>, 2010.
- Sosik, H. M., Olson, R. J., Neubert, M. G., Shalapyonok, A., and Solow, A. R.: Growth rates of coastal phytoplankton from time-series measurements with a submersible flow cytometer, *Limnol. Oceanogr.*, 48, 1756–1765, <https://doi.org/10.4319/lo.2003.48.5.1756>, 2003.
- Sterner, R. W. and Hessen, D. O.: Algal nutrient limitation and the nutrition of aquatic herbivores, *Annu. Rev. Ecol. Syst.*, 25, 1–29, 845 <https://doi.org/10.1146/annurev.es.25.110194.000245>, 1994.
- Talmy, D., Blackford, J., Hardman-Mountford, N., Polimene, L., Follows, M., and Geider, R.: Flexible C: N ratio enhances metabolism of large phytoplankton when resource supply is intermittent, *Biogeosciences*, 11, 4881–4895, <https://doi.org/10.5194/bg-11-4881-2014>, 2014.

- Thyssen, M., Tarran, G. A., Zubkov, M. V., Holland, R. J., Grégori, G., Burkhill, P. H., and Denis, M.: The emergence of automated high-frequency flow cytometry: revealing temporal and spatial phytoplankton variability, *J. Plankton Res.*, 30, 333–343, 850 <https://doi.org/10.1093/plankt/fbn005>, 2008.
- Thyssen, M., Grégori, G., Créach, V., Lahbib, S., Dugenne, M., Aardema, H., Artigas, L.-F., Huang, B., Barani, A., Beaugéard, L., et al.: Interoperable vocabulary for marine microbial flow cytometry, *Front. Mar. Sci.*, 9, <https://doi.org/10.3389/fmars.2022.975877>, 2022.
- Tzortzis, R., Doglioli, A. M., Barrillon, S., Petrenko, A. A., d'Ovidio, F., Izard, L., Thyssen, M., Pascual, A., Barceló-Llull, B., Cyr, F., Tedetti, M., Bhairy, N., Garreau, P., Dumas, F., and Gregori, G.: Impact of moderately energetic fine-scale dynamics on the phytoplankton 855 community structure in the western Mediterranean Sea, *Biogeosciences*, 18, 6455–6477, <https://doi.org/10.5194/bg-18-6455-2021>, 2021.
- Watson, A. J., Robinson, C., Robinson, J., Williams, P. I. B., and Fasham, M.: Spatial variability in the sink for atmospheric carbon dioxide in the North Atlantic, *Nature*, 350, 50–53, <https://doi.org/10.1038/350050a0>, 1991.
- Winder, M. and Cloern, J. E.: The annual cycles of phytoplankton biomass, *Philosophical Transactions of the Royal Society B: Biological Sciences*, 365, 3215–3226, <https://doi.org/10.1098/rstb.2010.0125>, 2010.
- 860 Worden, A. Z. and Binder, B. J.: Application of dilution experiments for measuring growth and mortality rates among Prochlorococcus and Synechococcus populations in oligotrophic environments, *Aquat. Microb. Ecol.*, 30, 159–174, <https://doi.org/10.3354/ame030159>, 2003.
- Zhang, Y., Jiao, N., and Hong, N.: Comparative study of picoplankton biomass and community structure in different provinces from subarctic to subtropical oceans, *Deep-Sea Res. Pt. II*, 55, 1605–1614, <https://doi.org/10.1016/j.dsr2.2008.04.014>, 2008.

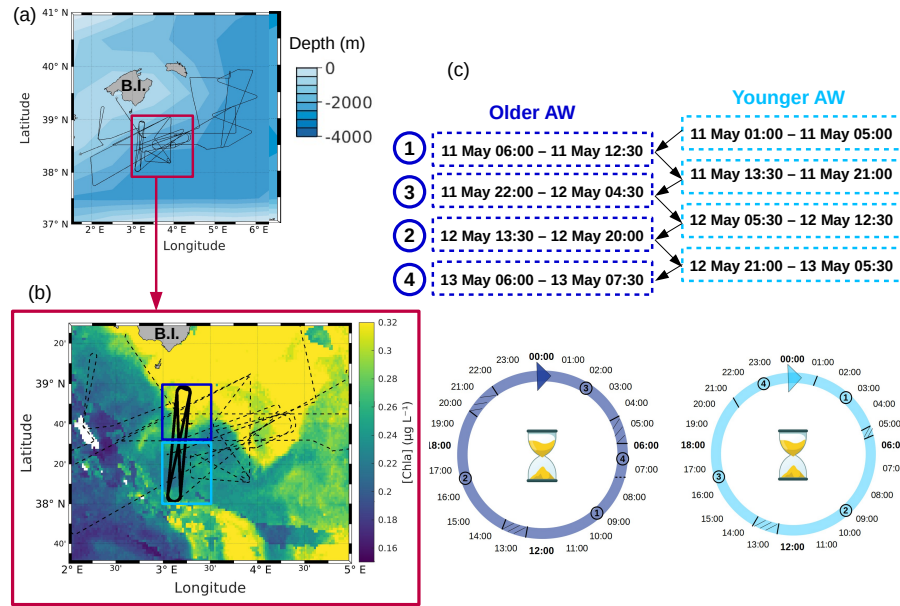


Figure 1. (a) Route of the RV *Beaupré* during the PROTEVSMED-SWOT cruise. The purple box encloses a (b) zoom of the sampling region with overlaid chlorophyll-a concentration ($\mu\text{g L}^{-1}$) of 11 May 2018. In panel (b) black dotted line represents the route of the ship and the bold black line represents the route of the Lagrangian sampling across the older AW (delimited by the box in dark blue) and the younger AW (delimited by the box in light blue). (c) Dates of the transects across the older AW and the younger AW, used to reconstruct a day of 24 h period in each water mass.

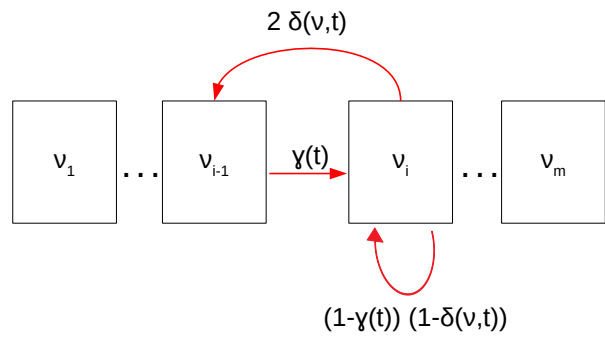


Figure 2. Cell cycle stages in the size-structured population model. Cells may grow to the next size class (γ) or be at equilibrium $(1 - \gamma(t))(1 - \delta(v, t))$. Above a particular size, cells are large enough to divide in two daughter cells with probability (δ) . Figure adapted from Sosik et al. (2003).

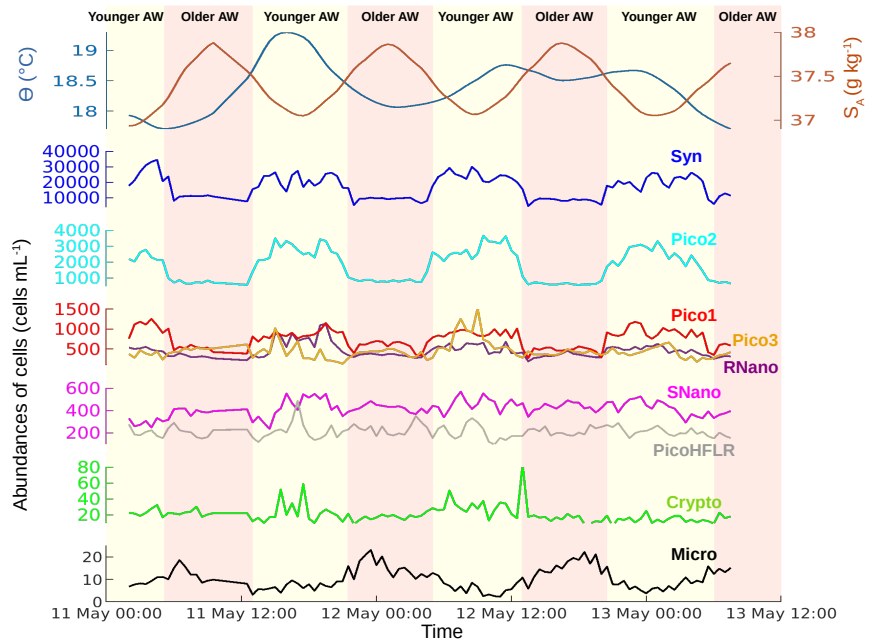


Figure 3. Temporal evolution of sea surface conservative temperature (Θ) in $^{\circ}\text{C}$, absolute salinity (S_A) in g kg^{-1} , and phytoplankton abundances in $\text{cells} \cdot \text{cm}^{-3}$ cells mL^{-1} , from 11 May 00:00 to 13 May 12:00 (UTC). Vertical colors correspond to the two water masses separated by the front (see Fig. 1).

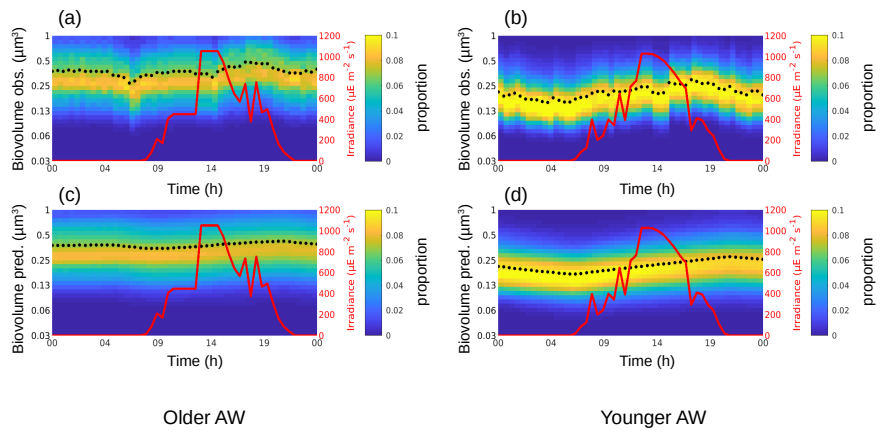


Figure 4. The background color represents the *Synechococcus* cell size distribution (i.e., biovolume in μm^3) observed (a, b) and predicted by the model (c, d) in the older AW (a, c) and in the younger AW (b, d) during 24 h. The black dots represent the mean of the biovolume (\bar{v}_{obs} and \bar{v}_{mod}) and the red line represents the irradiance ($\mu\text{E m}^{-2} \text{s}^{-1}$).

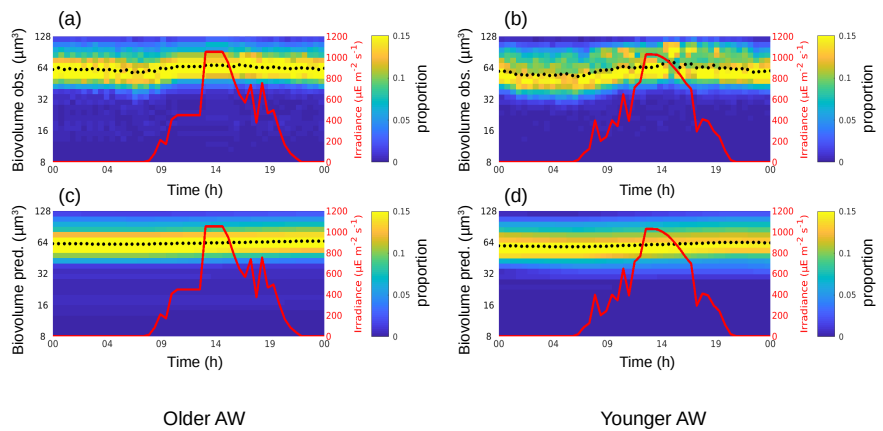


Figure 5. Same as Fig. 4 for RNano.

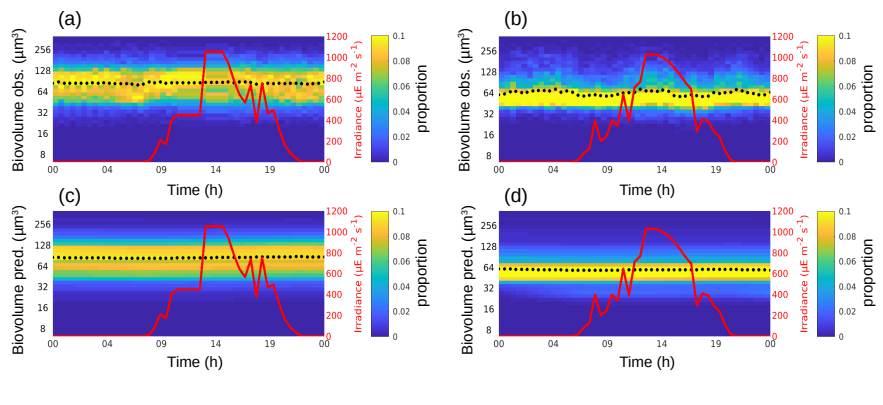


Figure 6. Same as Fig. 4 for SNano.

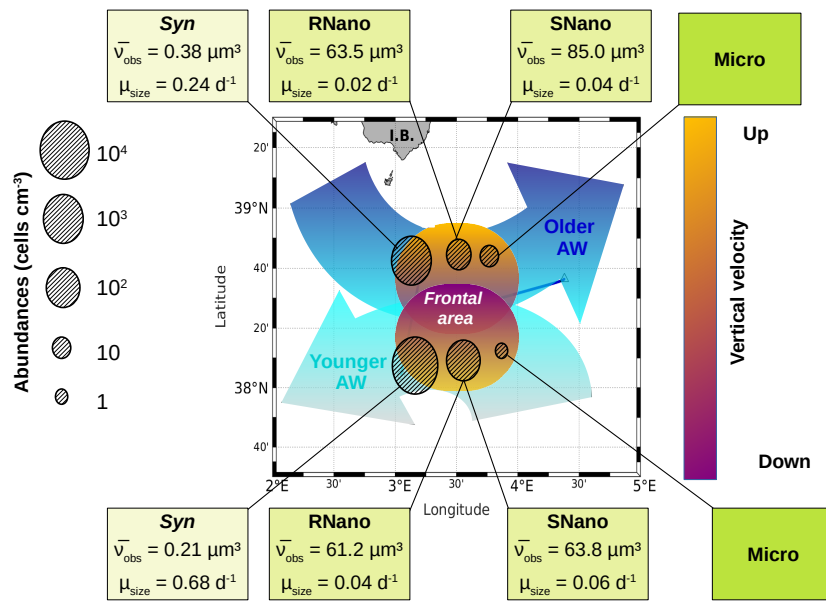


Figure 7. The contrasted distribution of phytoplankton in the frontal area. The circles represent the abundances of the several phytoplankton groups in the two water masses separated by the front. The boxes indicate the biovolume observed (\bar{v}_{obs}) and the growth rates (μ_{size}) for each phytoplankton group, as estimated from the model. Figure adapted from Tzortzis et al. (2021).

Table 1. Model parameters being optimized.

Parameters	Definition	Interval	Units
γ_{max}	Max proportions of cells in growing phase	$[0,1]$	\emptyset
E^*	Irradiance normalizing constant	$[0,\infty[$	$\mu\text{E m}^{-2} \text{s}^{-1}$
δ_{max}	Max proportions of cells in mitosis	$[0,1]$	\emptyset
\bar{v}	Mean of size density distribution	$[v_{min}, v_{max}]$	μm^3
σ_v	Standard deviation of size density distribution	$[10^{-06}, \infty[$	μm^3
\bar{t}	Mean of temporal density distribution	$[1, 24 \frac{1}{dt} + 1]$	hours
σ_t	Standard deviation of temporal density distribution	$[10^{-06}, \infty[$	hours

Table 2. Means of biovolumes observed (\bar{v}_{obs}) and modeled (\bar{v}_{mod}) in μm^3 , growth rates (μ_{size} , μ_{ratio} in d^{-1}) and loss rate (l , in d^{-1}) values for the phytoplankton groups, in the older and younger AW, as well as model fit parameters (see section 2.3). μ_{size} represents the PFG intrinsic growth rates (d^{-1}) and mean size ratio $\mu_{ratio} = \ln(v_{max}/v_{min})$ was calculated to provide an indication about the model performance and the synchronicity of populations (Dugenne et al., 2014).

	<i>Synechococcus</i>	RNano	SNano
Older AW	$\bar{v}_{obs} = 0.38 \pm 0.04$ $\bar{v}_{mod} = 0.38 \pm 0.02$ $\mu_{size} = 0.24 \pm 0.91$ $\mu_{ratio} = 0.59$ $l = 0.36$ $\sum(\theta) = 0.05$ $corr(\bar{v}_{obs}, \bar{v}_{mod}) = 0.60$	$\bar{v}_{obs} = 63.5 \pm 2.67$ $\bar{v}_{mod} = 63.5 \pm 1.79$ $\mu_{size} = 0.02 \pm 0.20$ $\mu_{ratio} = 0.17$ $l = 0.07$ $\sum(\theta) = 0.139$ $corr(\bar{v}_{obs}, \bar{v}_{mod}) = 0.46$	$\bar{v}_{obs} = 85.0 \pm 1.98$ $\bar{v}_{mod} = 84.7 \pm 1.38$ $\mu_{size} = 0.04 \pm 0.26$ $\mu_{ratio} = 0.11$ $l = 0.11$ $\sum(\theta) = 0.067$ $corr(\bar{v}_{obs}, \bar{v}_{mod}) = -0.05$
Younger AW	$\bar{v}_{obs} = 0.21 \pm 0.04$ $\bar{v}_{mod} = 0.22 \pm 0.03$ $\mu_{size} = 0.68 \pm 1.56$ $\mu_{ratio} = 0.63$ $l = 0.48$ $\sum(\theta) = 0.153$ $corr(\bar{v}_{obs}, \bar{v}_{mod}) = 0.65$	$\bar{v}_{obs} = 61.2 \pm 5.23$ $\bar{v}_{mod} = 60.6 \pm 2.17$ $\mu_{size} = 0.04 \pm 0.28$ $\mu_{ratio} = 0.33$ $l = -0.12$ $\sum(\theta) = 0.417$ $corr(\bar{v}_{obs}, \bar{v}_{mod}) = 0.56$	$\bar{v}_{obs} = 63.8 \pm 4.45$ $\bar{v}_{mod} = 59.1 \pm 0.61$ $\mu_{size} = 0.06 \pm 0.19$ $\mu_{ratio} = 0.24$ $l = 0.23$ $\sum(\theta) = 0.247$ $corr(\bar{v}_{obs}, \bar{v}_{mod}) = 0.15$

APPENDIX

865 Identification of the phytoplankton functional groups by flow cytometry

Up to 9 groups of phytoplankton have been identified on the cytograms (Fig. A1), thanks to their light scatter (forward scatter FWS, and sideward scatter SWS) and fluorescence intensities (red fluorescence FLR, and orange fluorescence FLO). These groups have been called using the conventional names used by flow cytometrists, i.e., some groups relate to taxonomy (*Synechococcus*, Cryptophytes) while others relate to a range of sizes (picoeukaryotes, nanoeukaryotes) as described by Sieburth et al. (1978). *Synechococcus* (Syn on Fig. A1c) is a prokaryotic picophytoplankton that can be distinguished from the other picophytoplankton owing to its high FLO intensity, induced by phycoerythrin pigment content. Cryptophytes (Crypto on Fig. A1c) were also discriminated from the other groups as they also produce a characteristic orange fluorescence induced by phycoerythrin. Concerning the other phytoplankton groups, 4 eukaryotic picophytoplankton groups were put in evidence: Pico1 (on Fig. A1c) characterized by lower FLR and FLO intensities than *Synechococcus*, Pico2 and Pico3 (on Fig. A1d) with higher FWS, SWS and FLR intensities than Pico1, PicoHFLR (on Fig. A1a) has a high FLR signal induced by chla. We defined 2 distinct nanophytoplankton groups (SNano and RNano) according to their high FLR and FLO intensities. SNano exhibits higher SWS/FWS ratio and SWS intensities than RNano (Fig. A1b and Fig. A1a). Finally, microphytoplankton (Micro) is characterized by the highest FLR and FWS intensities (Fig. A1c).

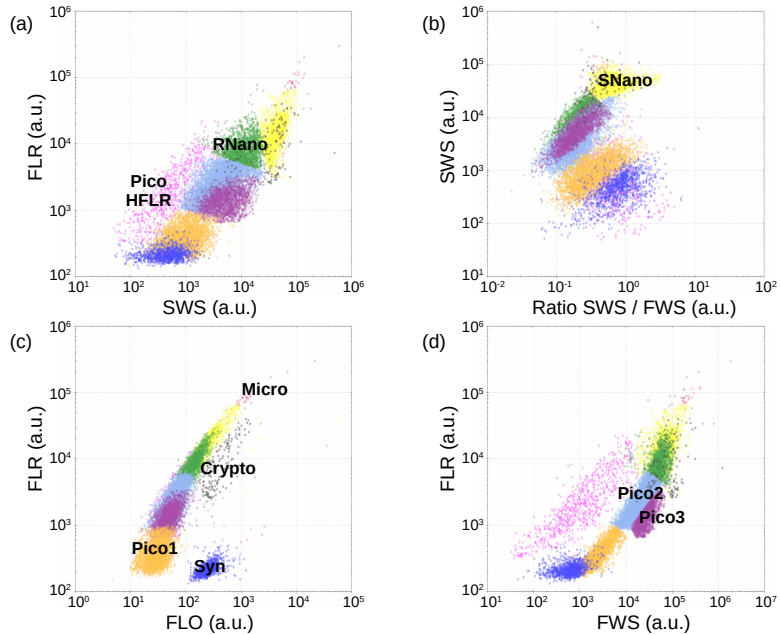


Figure A1. Cytograms obtained with the CytoSense automated flow cytometer. *Synechococcus* are in dark blue (Syn), the picophytoplankton with lowest FLO in orange (Pico1), the picophytoplankton with intermediate FWS in light blue (Pico2), the picophytoplankton with highest FWS in purple (Pico3), the picophytoplankton with a high red fluorescence in pink (PicoHFLR), the nanophytoplankton with high SWS/FWS ratio in yellow (SNano) and higher SWS intensities than the other nanophytoplankton (RNano) in green, the Cryptophytes in grey (Crypto) and the microphytoplankton in red (Micro). The flow cytometry units for both fluorescence and light scatter are arbitrary (a.u.). Figure extracted from Tzortzis et al. (2021).

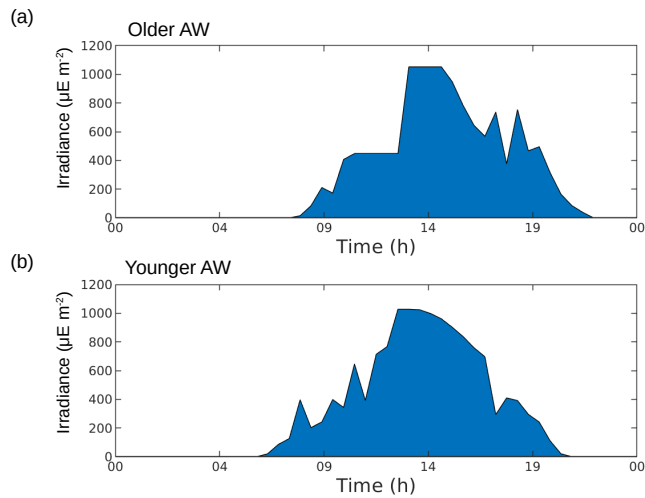


Figure A2. Reconstruction of irradiance during 24 h in the older AW (a) and the younger AW (b). Computation of trapezoidal integration of irradiance, in the older AW, $E1 = 286 \mu\text{E m}^{-2}$ and in the younger AW, $E2 = 299 \mu\text{E m}^{-2}$.

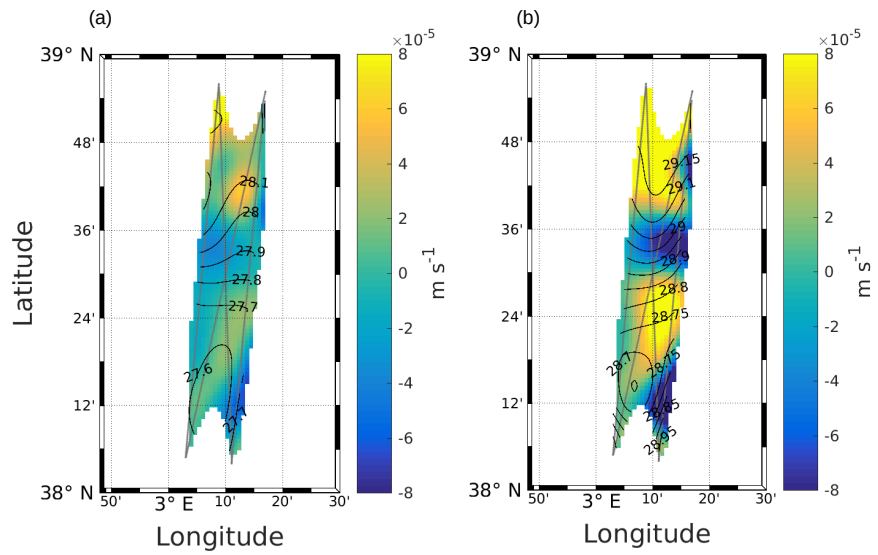


Figure A3. Vertical velocities at 25 m (a) and 85 m (b), calculated with the omega equation. Figure extracted from Tzortzis et al. (2021).